

CHARACTERIZATION OF THERMOSPHERIC NEUTRAL WINDS USING EMPIRICAL
MODELING AND OBSERVATIONAL VALIDATION

by

Patrick Bryan Dandenault
A Dissertation
Submitted to the
Graduate Faculty
of
George Mason University
in Partial Fulfillment of
The Requirements for the Degree
of
Doctor of Philosophy
Computational Sciences and Informatics

Committee:

_____	Dr. Philip Richards, Dissertation Director
_____	Dr. Jie Zhang, Committee (Chair)
_____	Dr. Dieter Bilitza, Committee Member
_____	Dr. Larry Paxton, Committee Member
_____	Dr. Robert Weigel, Committee Member
_____	Dr. Jason Kinser, Acting Director, Department of Computational and Data Sciences
_____	Dr. Donna M. Fox, Associate Dean, Office of Student Affairs & Special Programs, College of Science
_____	Dr. Peggy Agouris, Dean, College of Science
Date: _____	Summer Semester 2017 George Mason University Fairfax, VA

Characterization of Thermospheric Neutral Winds Using Empirical Modeling and
Observational Validation

A Dissertation submitted in partial fulfillment of the requirements for the degree of
Doctor of Philosophy at George Mason University

by

Patrick Bryan Dandenault
Master of Science
George Mason University, 2012
Master of Science
University of Mississippi, 1994
Bachelor of Science
Michigan State University, 1992

Director: Philip Richards, Professor
Department of Computational Sciences and Informatics

Summer Semester 2017
George Mason University
Fairfax, VA

Copyright 2017 Patrick Bryan Dandenault
All Rights Reserved

ACKNOWLEDGEMENTS

Thanks to everyone, for your patience.

TABLE OF CONTENTS

	Page
List of Tables.....	v
List of Figures	vi
Abstract.....	viii
Chapter 1: Introduction	1
Chapter 2: Background, Theory, and Implementation.....	10
2.1 Background.....	10
2.2 Theory	12
2.3 Wind Uncertainties.....	15
2.4 FLIP model.....	21
2.5 Implementation.....	22
Chapter 3: h_mF_2 , Ionosonde Data, and Geophysical Parameters.....	27
3.1 The Derivation of h_mF_2 Values.....	27
3.2 Ionosonde Databases.....	30
3.3 Geophysical Parameters	39
Chapter 4: Modeled Winds and Validation	44
4.1 Background.....	44
4.2 Validation of Equivalent Winds with Optical Wind Observations.....	46
4.3 Seasonal Comparisons	53
Chapter 5: Applied Research.....	58
5.1 The Midnight Collapse at Townsville, Australia	58
5.2 Tide power spectral densities	62
5.3 Model determination of the origin of the midnight collapse	68
5.4 Conclusions from the midnight collapse analysis	69
Chapter 6: Empirical Modeling.....	72
6.1 Empirical Modeling Formulation	72
6.2 Global Winds Database.....	82
6.3 Empirical Model Validation	87
6.4 Empirical Model User Interface.....	94
Chapter 7: Conclusion.....	99
Chapter 8: Future Work	103
References.....	105

LIST OF TABLES

Table	Page
Table 3.1. History of the ionosonde sites in the GIRO database.	39
Table 4.1. Geographic Latitude (LAT), Longitude (LON), and Magnetic Declination (BDEC) of the three Fabry-Pérot interferometers.....	46
Table 6.1. Location of the magnetic mid-latitude ionosondes that were used for basic research and to develop the new empirical equivalent wind model.....	84

LIST OF FIGURES

Figure	Page
Figure 1.1. Example of an ionospheric electron density profile.	2
Figure 2.1. HWM14 magnetic meridional wind speed vs. altitude at Boulder at 00:00 UT on Jan 1, 2012.	20
Figure 2.2. Observations and modeled values from Canberra, 1990.	25
Figure 3.1. Global Ionospheric Radio Observatory (GIRO) sites map.	31
Figure 3.2. Space Physics Interactive Data Resource (SPIDR) sites map.	31
Figure 3.3. 15-day seasonal median f_oF_2 values during 2014 from a digisonde and dynasonde (VIPR) co-located at Wallops Island.	34
Figure 3.4. 15-day seasonal median h_mF_2 values from the sites in Figure 3.3.	36
Figure 3.5. Number of stations vs. year in the SPIDR database.	37
Figure 3.6. Example of SPIDR data corruption.	38
Figure 3.7. (a) F10.7 and (b) F10.7A solar flux indices during the three decades used in this study. (c) Yearly mean total sunspot number from 1700 to 2016.	41
Figure 3.8. Distribution of the (a) 3-hour planetary Kp geomagnetic index, (b) F10.7 solar flux index, and (c) F10.7A solar flux index during the three decades used in this research.	42
Figure 3.9. Box-and-whisker plots for the (a) 3-hour Kp Index, (b) F10.7 solar flux, and (c) F10.7A solar flux values during the three decades used in this research.	43
Figure 4.1. Map showing the geographic location of the FPI sites.	47
Figure 4.2. (a) Winds, (b) h_mF_2 , and (c) N_mF_2 at each FPI site on March 23, 2014.	49
Figure 4.3. Thermospheric ion and electron temperatures from the FPI observations, FLIP model, and NRLMSISE-00 model for the same dates and times as Figure 4.2.	53
Figure 4.4. Observed and modeled seasonal (a, b, c, d) magnetic meridional neutral winds at PAR in 2014.	55
Figure 5.1. Observed and modeled data at Townsville during the 1974 spring equinox, March 18-31.	60
Figure 5.2. Power spectral density of the equivalent winds at Townsville for each equinox, every year from 1970 to 1980.	64
Figure 5.3. (a) March and September annual power spectral density of the diurnal, semidiurnal, terdiurnal and quatradiurnal components of the equivalent winds at Townsville (left panels). (b) March and September PSD ratios of the semidiurnal, terdiurnal and quatradiurnal components, relative to the diurnal component (right panels).	66

Figure 5.4. (a) Four sets of meridional winds, generated by bandpass-filtering the equivalent winds during the March 1977 equinox. The winds are obtained by successively allowing the DC component and the first four tidal components through the filter. (b) Three days of modeled $h_m F_2$ after using the four bandpass-filtered winds as inputs to FLIP.	69
Figure 6.1. An example of a Kriging semivariogram.....	76
Figure 6.2. A semivariogram range, sill, and nugget.....	78
Figure 6.3. Covariance equation used for kriging the equivalent winds at the 40 ionosonde sites to a global grid.....	79
Figure 6.4. (a) Equivalent winds at each of the 40 ionosonde sites. (b) Global modeled winds map after Kriging.	81
Figure 6.5. Map of the 40 ionosondes sites used to develop the new wind model. Ground-based sites are indicated with black circles.	85
Figure 6.6. Distribution of the $h_m F_2$ observations from the ground-based sites in Table 6.1.	85
Figure 6.7. $h_m F_2$ and meridional neutral winds at four locations during March 1-4, 1990.	88
Figure 6.8. MENTAT modeled winds, HWM14 winds, and FPI observed winds at the three sites used in Chapter 4.....	90
Figure 6.9. Observed and modeled seasonal (a, b, c, d) magnetic meridional neutral winds at PAR in 2014.....	92
Figure 6.10. Top: MENTAT modeled winds at Townsville (solid black line) and Arecibo (dashed red line) and HWM14 winds (stippled green line) at Townsville. Bottom: Modeled $h_m F_2$ when using the winds from the top plot as the input to the FLIP model.	94
Figure 6.11. Four days of modeled MENTAT winds using a 15-minute time resolution. .	97

ABSTRACT

CHARACTERIZATION OF THERMOSPHERIC NEUTRAL WINDS USING EMPIRICAL MODELING AND OBSERVATIONAL VALIDATION

Patrick Bryan Dandenault, Ph.D.

George Mason University, 2017

Dissertation Director: Dr. Philip Richards

An understanding of the coupling between the neutral winds of the thermosphere and the ionosphere is critical to understanding ionospheric dynamics. Measurements of upper atmospheric neutral air motion are required for any in-depth study of ionosphere-thermosphere coupling. The neutral wind is a major contributor to space weather through its effect on many of the observable quantities and physical processes of the ionosphere, including the density profiles of the ionospheric F region and the generation and maintenance of electric fields. The behavior of neutral winds is one of the most important and poorly known factors affecting the day-to-day variations in ionospheric electron and ion densities because it controls the whole electron density profile by altering the rate at which the ions diffuse along magnetic field lines. In fact, truly quantitative modeling of F region densities is not possible without an accurate

specification of neutral winds. Measured neutral winds are important for validating winds produced from general circulation models.

In the mid-latitude regions, thermosphere neutral winds are the primary driver of the altitude of the peak ionosphere (h_mF_2) due to the forcing of ionospheric plasma up and down Earth's magnetic field lines. In this thesis, we (1) optimized and validated a technique for deriving magnetic meridional thermospheric neutral winds using h_mF_2 observations from bottomside sounders. Compared derived neutral winds from ionosonde data were compared with wind observations from Fabry-Pérot interferometers (FPI) in order to adjust the model parameters to regularly generate physically-realistic winds. This technique was then used to (2) investigate the rate and causes of the sudden descent (midnight collapse) of the ionosphere h_mF_2 at Townsville, Australia over a ten-year period. The study included a harmonic analysis of the tidal components of the meridional neutral winds in order to study long-term trends and how the individual wind tides may contribute to the collapse of h_mF_2 . A global database of ionosonde observations spanning three decades was then used to (3) develop a new model of the horizontal equivalent neutral winds in the mid-latitude regions.

The result of task (1) was a new, consistent method for regularly generating realistic meridional neutral winds from h_mF_2 observations in the mid-latitude regions. The modeled winds compared well with FPI wind observations and performed better than another thermospheric neutral wind model. The application of this method in task (2) determined that the diurnal (24-hour), semidiurnal (12-hour), and terdiurnal (8-hour)

tidal components of the meridional neutral wind all play a significant role in the regular midnight collapse of the ionosphere at Townsville, but the effect of the quadradiurnal (6-hour) wind component was minimal. A spectral analysis of the tidal wind components over the full decade revealed that the relative strength of wind tides varies widely with solar flux and that the terdiurnal wind component becomes dominant during solar maximum. Task (3) resulted in the generation of a new empirical wind model that generates neutral winds as a function of the year, day of year, solar local time, solar flux, and geographic latitude and longitude. The new empirical winds compared well with FPI wind observations over short time periods and performed well (statistically) with the observed winds over four seasonal 30-day periods spanning an entire year. The new model also matched wind observations better than the current most widely-used thermospheric wind model, and it accounts for changes in the solar flux, which the other model does not yet do.

CHAPTER 1: INTRODUCTION

The thermosphere is a layer of Earth's atmosphere that extends from about 90 km to between 500 and 1,000 km in altitude. Although the thermosphere is part of Earth's atmosphere, the air density is so low in this layer that most of it is what we normally think of as outer space. In the thermosphere and above, gas particles collide so infrequently that the gases become distributed due to gravitational stratification and the types of chemical elements they contain. High-energy X-rays and ultraviolet (UV) "light" from the Sun are constantly colliding with gas atoms and molecules in the thermosphere. Some of these collisions knock electrons free from the atoms and molecules, creating electrically charged ions and free electrons. These electrically charged ions and electrons move and behave differently than neutral atoms and molecules. Regions with higher concentrations of ions and free electrons form a region within the thermosphere known as the ionosphere.

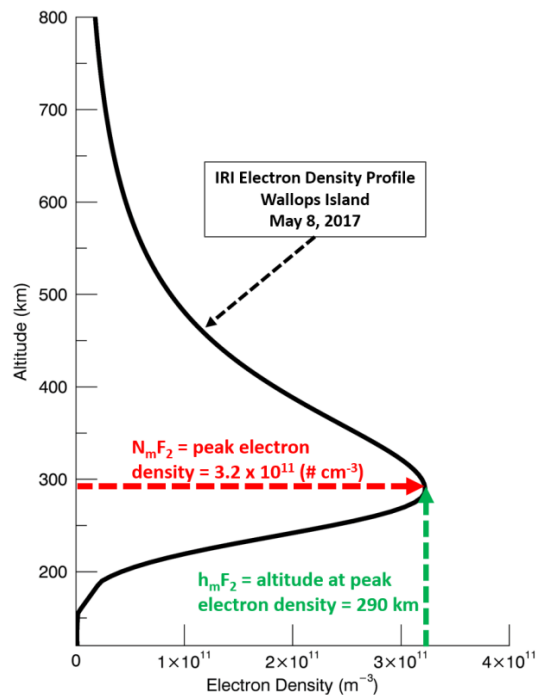


Figure 1.1. Example of an ionospheric electron density profile. The peak electron density value, $N_m F_2$, is shown using the red dashed horizontal line. The altitude at which $N_m F_2$, occurs, known as $h_m F_2$, is shown using the green vertical dashed line.

An ionospheric electron density profile is shown in Figure 1.1. There are three main vertical regions of the ionosphere, called the D region, the E region, and the F region. These regions do not have sharp boundaries, and the altitudes at which they occur vary over the course of a day and from season to season. The D region is the lowest, starting at an altitude of 60 or 70 km and extending upward to about 90 km. Next higher is the E region, starting at about 90 or 100 km and extending to 120 or 150 km. The uppermost part of the ionosphere, the F region, begins at about 150 km and can extend to altitudes as high as 500 km. The F region can be further subdivided into two sub regions, with the lower layer known as the F1 region and the upper layer known

as the F2 region. The F1 region below 200 km is dominated by molecular ions while the F2 region above 200 km is dominated by atomic oxygen ions but the maximum electron density typically occurs in the upper F2 region. The peak electron density value within the ionospheric F2 region is denoted using the term N_mF_2 , and the altitude at which the peak electron density (N_mF_2) occurs at is known as the height of the maximum F2 layer, and is denoted using the term h_mF_2 .

The thermosphere is in motion on all spatial and temporal scales. During magnetically quiet periods, upper thermospheric neutral (not electrically charged) winds generally blow from the (hotter) high-pressure area located directly beneath the sun on the Earth's dayside to the antipodal (cooler) lower-pressure region around midnight. This global pressure difference generates a meridional wind pattern at mid-latitudes that is predominantly poleward during the day and equatorward at night. These neutral winds interact with the ionized atmosphere and force it to move in the same horizontal direction due to drag. Although the motion of the neutral winds is predominantly horizontal, the motion of charged particles (ions) are constrained to move parallel to Earth's magnetic field lines. The result is that the charge particles will move horizontally due to forcing from neutral winds, but they will also move vertically due to the vertical inclination of magnetic field lines. The resulting poleward/equatorward winds lower/raise the altitude of the peak ionosphere (h_mF_2) due to the local inclination angle of Earth's magnetic field lines.

During magnetic storms, the increased energy deposition from Joule heating and convective ion drifts acts to oppose the poleward winds on the dayside and enhance the equatorward winds on the night side. Impulsive events in the auroral regions may also lead to atmospheric waves known as traveling ionospheric disturbances (TIDs) that propagate from the poles toward the equator. Thus, magnetic activity leads to day-to-day variability in thermospheric wind patterns.

The influence of thermosphere neutral winds on the ionosphere is critical to understanding ionospheric dynamics. While the measurements of many of the properties of the ionosphere can be made reliably using radio propagation, radar techniques, and optical techniques, measurements of the properties of the neutral thermosphere are difficult. Measurements of upper atmospheric neutral air motion are required for any in-depth study of ionosphere-thermosphere coupling. The neutral winds affect many of the observable quantities and physical processes of the ionosphere, including the density profiles of the ionospheric F region and the generation and maintenance of electric fields. The behavior of neutral winds is one of the most important but poorly known factors affecting the day-to-day variations in ionospheric electron and ion densities because it controls the whole electron density profile by altering the rate at which the ions diffuse along magnetic field lines. Accurate quantitative modeling of F region densities is not possible without an accurate specification of neutral winds in the thermosphere. In addition, general circulation models need neutral wind data for validation.

Day-to-day variations of the ionosphere may also result from waves from the lower atmosphere. For example, the semi-diurnal tide has a strong signature in the ionosphere at low latitudes [Crary and Forbes, 1986; Richards and Wilkinson, 1998]. *Immel et al.* [2006] proposed that the observed 1000-km scale longitudinal variation in ionospheric densities may vary with the strength of atmospheric tides that are driven by weather in the tropics. *Crary and Forbes* [1986] found that both the semidiurnal and terdiurnal waves were important for explaining the so-called midnight collapse of the ionosphere over Arecibo, Puerto Rico. At least part of the day-to-day variability in the ionosphere may be due to the combined effects of these waves with different periods. These effects may be captured in an empirical model of thermospheric neutral winds if the observational database is large enough and it spans the appropriate lengths of time.

This research employs a method to derive the meridional component of equivalent neutral winds in the thermosphere from values of $h_m F_2$ derived from ionosonde measurements. The winds obtained from $h_m F_2$ are termed 'equivalent' or 'effective' neutral winds because they comprise both neutral wind and electric field contributions to changes in $h_m F_2$ [Rishbeth, 1972]. The method has been shown to produce winds with comparable accuracy to other techniques and it has the advantage of being able to obtain winds both day and night and at the many mid-latitude ionosonde sites. The numerical technique has been developed over the past 20 years [Miller et al., 1986; 1993; Richards, 1991; Dyson et al., 1997, Richards et al., 2009]. The technique makes use of the Field Line Interhemispheric Plasma (FLIP) model of the

ionosphere [Richards *et al.*, 2001], which is described later. The findings of this research provide an improved understanding of thermospheric winds and the resulting empirical wind model will be a useful tool for ionospheric researchers.

Empirical models have proven to be extremely important to progress in space science. They serve to summarize the variability of the measurements and provide values at times and locations where there are limited or no observations. They are widely used as inputs to other types of models as well as serving as benchmarks for the validity of physics-based models. Some of most cited papers in the ionosphere-thermosphere literature are those that describe the Mass-Spectrometer-Incoherent-Scatter (MSIS) neutral atmosphere model [Hedin, 1983, 1987]. Picone *et al.* [2002] later upgraded the MSIS model to version NRLMSISE-00. The upgraded model provides reliable neutral densities for the calculation of ionospheric densities and airglow emission rates, but it also has been used to provide initial and lower boundary conditions for other models and to validate the output of general circulation models.

The Horizontal Wind Model (HWM) series of empirical neutral wind models [Hedin *et al.*, 1988; 1991; 1996; Drob *et al.*, 2008; 2015] have been developed to describe horizontal winds in the troposphere, stratosphere, mesosphere, and thermosphere. Over the years, the HWM models have used satellite, rocket, radar, interferometer, and other wind measurements to provide constraints to its empirical wind specifications. HWM has the potential to emulate the success of the MSIS models, but it currently lacks sufficient coverage across the model parameter space (e.g.

geographic regions, solar cycle, season, local time). Historically, the most widely used empirical wind model has been the HWM93 model [Hedin *et al.*, 1996]. Although this model has been implemented extensively, its accuracy is limited because it was based on a limited amount of data, especially in the Southern Hemisphere [Hedin *et al.*, 1996]. The most recent version, HWM14 [Drob, 2015] shows dramatically improved agreement with the available data over that of the previous version, HWM07, due to the increased amount of observations and improvements in the formalism. The large majority of the HWM data sets are from the northern hemisphere; fewer data are available from the southern hemisphere. As a result, the HWM winds are extrapolated to regions that may not be well represented in its observational database [see Richards *et al.*, 2017 for a discussion]. The empirical equivalent wind model that is developed in this research uses a database with a large global distribution, spans a much longer period, and contains uniform temporal observations at a high (1-hour) cadence. These new modeled wind data will improve our understanding of the causes of day-to-day dynamics of the ionospheric electron density by establishing a vital baseline from which both short and long-term variabilities may be investigated.

A significant advantage of equivalent winds over other potential sources for investigating thermospheric wind dynamics during geomagnetic storms and their influence on the coupled magnetosphere-ionosphere-thermosphere system is their 24 hours per day coverage and there is a long-standing global network of stations with data spanning more than five decades. This enables thermospheric wind behavior to be

studied on many different time scales that result from solar and magnetic activity and tidal forcing from below. For example, an analysis of the equivalent winds from Townsville, Australia (20°S, 147°E) indicates that the semi-diurnal component is dominant with smaller contributions from the diurnal and ter-diurnal components, while just to the south at Brisbane (27°S, 153°E), the diurnal component is dominant [Dandenault and Richards, 2015]. Such variability is difficult to reliably extract from other data sets because of their poor temporal and spatial characteristics. Although the ionosonde database is large and has the required temporal attributes for studying solar cycle, season, diurnal, and hourly variability, the spatial coverage is still limited to approximately 50 ground-based ionosondes.

The benefit of this research is that it advances the understanding of the fundamental physical processes of the space environment from Earth to the sun, and from the sun to other magnetized planets. It should also improve progress in understanding how human society, technological systems, and the habitability of planets are affected by solar variability interacting with planetary magnetic fields and atmospheres. The ionosonde data and equivalent winds could also be used to fine-tune global circulation thermospheric models before a disturbance is detected in interplanetary space, by running the models several days out to predict possible effects when a disturbance reaches Earth.

Chapter 2 focuses on the historical background and theory behind this research and its practical implementation. Chapter 3 discusses the generation of $h_m F_2$ layer

height values, the various global ionosonde data sets, and the geophysical conditions during the time span of the ionosonde database. Chapter 4 discusses the modeled equivalent winds at individual locations and includes examples of validation with wind observations. Chapter 5 describes the findings of a basic research paper that used these methods to investigate the midnight collapse of the ionosphere at Townsville, Australia. Chapter 6 discusses the global equivalent neutral winds database, the formulation and design of a new empirical wind model, validations of the empirical model with wind observations, and an overview of model's user interface. Chapter 7 provides conclusions, and chapters 8 and 9, respectively, include possible future work and the citations for this effort.

CHAPTER 2: BACKGROUND, THEORY, AND IMPLEMENTATION

2.1 Background

The concepts behind deriving meridional neutral winds from the ionospheric F_2 peak heights has been around for more than five decades. *Rishbeth and Barron* [1960], *Rishbeth* [1966, 1967, 1972, 1978] and *Hanson and Patterson* [1964] showed that if the external forcing from the neutral atmosphere is not too great, there is a linear relationship between $h_m F_2$ and the horizontal neutral wind speed. A comprehensive review of thermospheric winds in the F-region was presented by *Rishbeth* [1972]. *Rishbeth* [1967] compared the behavior of the F_2 region under the influence of a meridional wind to an error-sensing negative feedback “servo” system and developed the equations describing the rate of vertical movement of the F_2 layer and the equilibrium position of its peak density. According to the servo model, an equatorward wind will retard the downward flow of plasma, causing the electron density to peak at a higher altitude. On the other hand, a poleward wind increases the downward diffusion, causing the electron density to peak at a lower altitude. A linear relationship holds approximately between the flow of horizontal neutral winds and the resulting change in the height of the F-layer peak when wind speeds are moderate and electric fields are

small [Rishbeth and Barron, 1960; Hanson and Patterson, 1964; Rishbeth, 1966; Buonsanto, et al, 1989].

Using the FLIP model, Miller et al. [1986] determined the constant of proportionality for the approximate linear relationship between changes in $h_m F_2$ and the horizontal neutral wind speed, which along with the peak height in the absence of a neutral wind provides a means for ionospheric modelers to reproduce the observed height with reasonable precision. However, this method is unable to produce rapid changes in wind speed because it implicitly assumes an infinite time for $h_m F_2$ to adjust to changes in the neutral wind. The procedure was also complicated and time consuming for routine use because it required three FLIP model simulations to model $N_m F_2$.

Richards [1991] introduced a new approach to the servo model that reduces the complexity and computational requirements and more accurately reproduces the observed ionospheric heights. The improvement was achieved by using the FLIP model to estimate the wind that is needed to reproduce the observed height at the next time step using the calculated height and wind at the current time step. With this technique, the winds are continuously adjusted to bring the calculated height into better agreement with the observed height during a time-dependent simulation. With this method only one FLIP model run is required to model $N_m F_2$. As will be shown, the winds from the new algorithm agree very well with optical and radar ground-truth observations. With the ability to accurately and quickly reproduce observed F_2 layer heights, it is possible to study the causes of variations in the peak electron density

($N_m F_2$). Since modern ionosonde data sets are so large and distributed globally, it is now possible to develop a new empirical model of the equivalent meridional neutral winds based entirely on ionosonde $h_m F_2$ observations.

2.2 Theory

The underlying principle of the simple servo model is straightforward [Rishbeth, 1974]. The relationship between the horizontal component of the neutral wind velocity (U) along a magnetic meridian and the resulting change in height of the F layer peak (Δh) can be written as

$$\Delta h = \alpha \Delta U \quad (1)$$

In the algorithm developed by *Miller et al.* [1986, 1989] the diurnal variation of the constant of proportionality is determined by modeling the diurnal variation of the F region for two different wind speeds using a time dependent ionospheric model for the specific location, time, and solar conditions.

$$\alpha(t) = \frac{(h_1(t) - h_2(t))}{U_1(t) - U_2(t)} \quad (2)$$

where $h_1(t)$ is the calculated height of the F_2 layer peak for $U = U_1(t)$ at time t and $h_2(t)$ is the calculated height of the F_2 layer peak for $U = U_2(t)$ at time t . Note that the peak heights and the winds in (2) are calculated by a model. In what follows, the measured

height is referred to as $h_m F_2$. Using $\alpha(t)$ from (2) along with the measured $h_m F_2$, the *Miller et al.* [1986, 1989] derived the following expression for the equivalent neutral wind

$$U(t) = \frac{(h_m F_2(t) - h_0(t))}{\alpha(t)} \quad (3)$$

where $h_0(t)$ is the natural altitude from where the wind speed is zero and is called the balance height. The *Miller et al.* technique requires 3 runs of the FLIP model to determine the equivalent wind as a function of time.

Richards [1991] showed that the computation time of the time dependent ionospheric model could be reduced by two thirds and the accuracy of the modeled $h_m F_2$ improved by calculating the equivalent wind at the next time step in a single run. As presented by *Richards* [1991], equation (3) can be written for time $(t + \Delta t)$ as

$$U(t + \Delta t) = \frac{(h_m F_2(t + \Delta t) - h_0(t + \Delta t))}{\alpha(t + \Delta t)} \quad (4)$$

Both $\alpha(t)$ and $h_0(t)$ are well-behaved and slowly varying functions of time so that, for small Δt , (4) can be approximated by

$$U(t + \Delta t) = \frac{(h_m F_2(t + \Delta t) - h_0(t))}{\alpha(t)} \quad (5)$$

Subtracting (3) from (5) gives

$$U(t + \Delta t) = \frac{(h_m F_2(t + \Delta t) - h_m F_2(t))}{\alpha(t)} + U(t) \quad (6)$$

Although the measured wind $U(t)$ corresponding to the measured $h_m F_2$ is not available, the calculated wind $U'(t)$ corresponding to the calculated $h'(t)$ is available, and $h'(t)$ and $U'(t)$ are related to the true values by the following relationships:

$$h_m F_2(t) = h'(t) + \Delta h'(t) \quad (7)$$

$$U(t) = U'(t) + \Delta U'(t) \quad (8)$$

where $\Delta h'(t)$ is the displacement from the true height resulting from an error $\Delta U'(t)$ in the wind. Substituting equations (7) and (8) into equation (6) yields

$$U(t + \Delta t) = \frac{(h_m F_2(t + \Delta t) - h'(t))}{\alpha(t)} + U'(t) - \frac{\Delta h'(t)}{\alpha(t)} + \Delta U'(t) \quad (9)$$

Using the relationship from (1) $\Delta U' = \frac{\Delta h'}{\alpha}$, the last two terms in (9) sum to zero and we are left with

$$U(t + \Delta t) = \frac{(h_m^{F_2}(t+\Delta t) - h'(t))}{\alpha(t)} + U'(t) \quad (10)$$

where $h'(t)$ is the calculated height of the F_2 layer and $U'(t)$ is the equivalent neutral wind at time t .

Note that information about $h_o(t)$ is implicit in the calculated values of $h'(t)$ and $U'(t)$. Equation (10) follows from (3) under the assumption that $h_o(t)$ and $\alpha(t)$ are constant for small time steps. *Buonsanto et al.* [1997] and *Dyson et al.* [1997] showed that the time constant for changes in the layer height due to changes in the neutral wind is on the order of 15 minutes. The FLIP model is typically run with a 5-minute time resolution to characterize the ionospheric specification and dynamics, so it is reasonable to assume that $h_o(t)$ and $\alpha(t)$ will be constant for such model runs.

2.3 Wind Uncertainties

All methods for the determination of neutral winds in the thermosphere have their limitations. Current techniques for measuring thermospheric wind speeds include ground-based incoherent scatter radar (ISR) and optical Fabry-Perot interferometers (FPI). The ISR uses doppler-shifted radar echoes from a local plasma wind to determine collocated neutral wind speeds. The FPI analyzes doppler-shifting of 6300 Å naturally-occurring nighttime airglow to determine neutral wind speeds. Accurate ground-based optical measurements can only be made on clear moonless nights, OH contamination can be significant, airglow brightness gradients can create biased wind data, low nighttime electron densities create low signal-to-noise ratios which limit the accuracy of

retrievals, and there are still a limited number of observation sites. Radar measurements are only available for limited periods of time and there are few observation sites. Satellite measurements have the potential to provide good global coverage but there are still relatively few measurements in the F-region.

The derivation of equivalent winds from $h_m F_2$ has the benefits of an extensive global database with hourly long-term coverage, but this technique has three primary limitations and two minor limitations. None of these limitations are serious because several previous studies have shown good agreement between equivalent winds and both radar and optical winds [e.g. *Dyson et al*, 1997; *Buonsanto et al.* [1997]; *Richards et al.*, 2009].

The first limitation is that only neutral winds along the local magnetic meridian are obtained because winds perpendicular to the magnetic meridian do not cause vertical ion motion. This is not a serious problem for calculating day-to-day ionospheric density variations since only the magnetic meridional component of the wind is important.

Second, the equivalent wind method only works well at mid-latitudes for two reasons, 1) because Earth's magnetic field lines are nearly horizontal in the equatorial region and nearly vertical in the polar regions, the neutral winds cannot significantly affect $h_m F_2$ because the vertical component of the wind velocity is too small, 2) convection electric fields can be large in the auroral and equatorial regions.

Third, there is uncertainty in the magnitude of the O⁺-O collision frequency (ion drag). A large value of the collision frequency will cause increased drag between ions and neutrals and therefore smaller calculated neutral winds speeds. By comparing winds from optical and radar measurements, *Burnside et al.* [1987] proposed that the collision frequency of *Schunk and Walker* [1973] should be increased by a factor of 1.7. This factor came to be known as the Burnside factor [*Salah*, 1993]. *Buonsanto et al.* [1997b] reviewed the collision frequency problem and used optical and radar data to determine a revised multiplicative factor of 1.2 to 1.4. *Nicolls et al.* [2006] used the ionospheric energy balance to determine a Burnside factor of 1.26 ± 0.02 . Different ionosphere models use different collision frequencies. However, for ionospheric modeling, the important consideration is that the ionospheric model is consistent with the Burnside factor used in the construction of the wind model, and it is trivial to change the Burnside factor with FLIP model runs. Since the radar community settled on a value of 1.3 for their analyses and the well-known Horizontal Wind Model (HWM) uses those radar data, we use a value of 1.3 for the generation of winds for the equivalent winds database.

There are relatively brief periods near sunrise where this method can be less accurate, especially at solar minimum when pre-dawn electron densities are low. This issue is associated with the layer height at that local time not being in equilibrium as discussed later in this chapter. Finally, the equivalent winds may contain vertical drifts due to horizontal electric fields. The vertical influence of East-West electric fields due to

$\vec{E} \times \vec{B}$ drift on the height of the ionosphere cannot be differentiated from the vertical influence of meridional neutral winds. To compare equivalent winds with other methods, electric fields would be needed, but their measurement are even less available than neutral winds. This means that a digisonde would need to be collocated with an incoherent scatter radar and an optical instrument. Such a situation was available in the March 1990 for the study of *Richards et al.* [1994] at Millstone Hill and Arecibo and there was very good agreement between the radar, optical, and equivalent wind methods without considering electric fields. Electric fields are expected to be small in the magnetic mid-latitudes.

Gravity waves that could reach the thermosphere from below have also been considered as a potential source of error, but they have periods less than one hour [Fritts and Vadas, 2008] and would appear in the data as relatively small random fluctuations in $h_m F_2$. Vertical winds from below that affect the F_2 layer height could influence the derived equivalent winds, but such winds are highly variable and rarely reach bottomside F layer altitudes [Larsen, 2002; Larsen and Meriwether, 2012]. Therefore, the effects of gravity waves and vertical winds appear as rare, random day-to-day variations in $h_m F_2$ and are not important factors in this research.

The primary error in the derivation of the meridional neutral winds is the uncertainty of the observed F_2 layer heights. The technique developed by *Dudeney* [1983] for estimating $h_m F_2$ was shown to be accurate to within 4% to 5% at magnetic mid-latitudes. If the measured layer height is systematically too high, the calculated

winds and peak electron densities will also be too high. Random errors in the measured height are not critically important for overall wind speeds and electron density values because the ionospheric model acts as a self-correcting function. Non-systematic observational errors in h_mF_2 at one time step will be compensated for by observations of h_mF_2 in subsequent time steps.

Because the equivalent winds are obtained at h_mF_2 , they automatically capture any altitude variation of the winds. The altitude variation is expected to be small because viscosity is very large above ~ 220 km [Rishbeth, 1972]. Any altitude variation of the winds would only cause a problem if the winds are used in an ionospheric model under different thermospheric conditions from which they were obtained. This is most likely to happen if the equivalent winds were obtained under quiet magnetic conditions but were erroneously applied under disturbed conditions because the balance heights would be different. The three-hour planetary Kp Index is used to characterize the magnitude of a geomagnetic disturbance. Kp is an integer in the range 0-9, with values 0-3 representing periods of quiet geomagnetic activity, and values 4-9 indicating periods with disturbed geomagnetic activity and a geomagnetic storm. FLIP model calculations show that even when conditions go from quiet (Kp=1) to disturbed (Kp=5) the altitude difference is generally less than 5 km in the daytime and less than 25km at night. Note that winds obtained from radar and optical measurements suffer the same problem when applied to different conditions. In fact, optical measurements always come from

about ~ 60 km below $h_m F_2$, making them less desirable for ionospheric models if there are large vertical gradients.

An indication of the possible altitude variation of neutral winds can be obtained from the HWM14 model. Figure 2.1 shows the modeled range of meridional wind speed at Boulder at 00:00 UT on January 1, 2012 as a function of altitude. The shaded green area in the plot shows the estimated range error for $h_m F_2$ ($264 \text{ km} \pm 5\%$). Within that range of $h_m F_2$, the possible range of meridional wind speeds may be estimated by the region in which the thick wind speed curve intersects the shaded green area. The result suggests that an $h_m F_2$ observation with 5% error corresponds to a wind speed variance of ~ 6 m/s. So, if the HWM14 altitude variation is correct, the assumption of no altitude variation causes little error for ionospheric models.

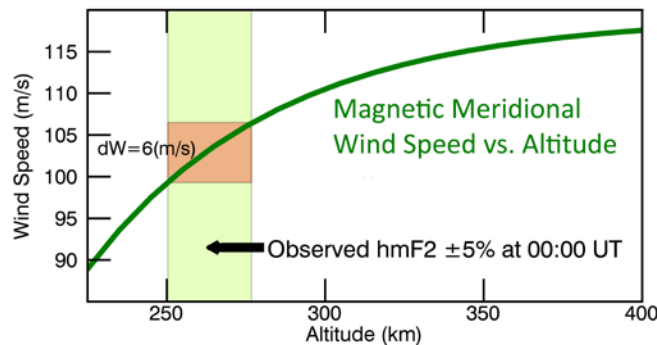


Figure 2.1. HWM14 magnetic meridional wind speed vs. altitude at Boulder at 00:00 UT on Jan 1, 2012.

2.4 FLIP model

The algorithms required to derive the equivalent meridional neutral winds from $h_m F_2$ observations have been fully integrated into the Field Line Interhemispheric Plasma (FLIP) model. FLIP is one-dimensional first-principles physics model that calculates plasma densities and temperatures along entire magnetic flux tubes from 80 km altitude in the northern hemisphere, through the plasmasphere, to 80 km altitude in the southern hemisphere. The basis for the model has been described previously by *Richards and Torr* [1988] and by *Torr et al.* [1990]. The He^+ chemical and physical processes have been discussed by *Newberry et al.* [1989]. It uses a tilted dipole approximation for the Earth's magnetic field that varies with longitude to produce good agreement with the International Geomagnetic Reference Field (IGRF) model. The magnetic declination and inclination are specified directly from the IGRF model.

The continuity and momentum equations are solved for O^+ , H^+ , and He^+ , as formulated for the topside ionosphere by *St. Maurice and Schunk* [1976]. Collisions between atmospheric ions and neutrals (ion drag) have been included to extend the equations into the E and F regions of the ionosphere. The electron and ion temperatures are obtained by solving the energy equations [*Schunk and Nagy*, 1978]. Electron heating due to photoelectrons is provided by a solution of the two-stream photoelectron flux equations using the method of *Nagy and Banks* [1970]. The solutions have been extended to encompass the entire field line on the same spatial grid as the ion continuity and momentum equations. Using the latest cross sections and solar EUV

fluxes as inputs, *Richards and Torr* [1984] demonstrated that the model photoelectron fluxes were in good agreement with the measured fluxes of *Lee et al.* [1980]. The FLIP model includes an option to calculate the vibrational distribution of N_2 to consider the strong dependence of the $[O^+ + N_2 \rightarrow NO^+ + N]$ reaction rate on the degree of vibrational excitation of N_2 . It has been shown by *Richards et al.* [2010] that this effect is most important at solar maximum in summer and during magnetic storms.

To specify the physics of the ionosphere, the FLIP model requires three key inputs: (1) the solar EUV flux; (2) a specification of the neutral atmosphere; and (3) the meridional component of the neutral wind. Normally, ionosphere models use empirical wind models or sometimes ingest observed winds. The FLIP model can do this too, but its most accurate mode of operation is to read $h_m F_2$ from an input file and use the algorithm in Equation (11) to determine magnetic meridional equivalent neutral winds. In the absence of $h_m F_2$ observations, it can use the IRI model to provide $h_m F_2$.

2.5 Implementation

In this dissertation, the above technique, along with $h_m F_2$ data from a massive repository of ionosonde observations, is used to develop a global database of equivalent neutral winds. The resulting database of winds is then used to develop a new empirical horizontal neutral wind model called MENTAT, which stands for Magnetic mEridional NeuTrAl Thermospheric wind model. The raw equivalent wind output from the FLIP model can have overly large variability due to random errors in the measured $h_m F_2$. For example, a 10 km error in $h_m F_2$ could lead to a 20 m/s error in wind at night. If the $h_m F_2$

errors are truly random, the FLIP model is self-correcting. The MENTAT winds are a higher-level data product and exhibit the same general variability as the raw FLIP winds, but they have been range limited, median filtered and smoothed using boxcar-averaging. Median filtering was used to suppress data outliers and wind speeds were limited to maximum of ± 250 m/s. The algorithm used for boxcar smoothing is shown below and used a 3-hour window:

$$R_i = \frac{1}{w} \sum_{j=0}^{w-1} A_{i+j-\frac{w}{2}} \quad \text{if } \frac{(w-1)}{2} \leq i \leq N - \frac{(w+1)}{2} \quad (12)$$

otherwise $R_i = A_i$ N is the number of elements in the array A .

Figure 2.2 shows an example of $h_m F_2$ layer heights, and FLIP and HWM14 model winds at Canberra (35°S, 149°E) for the year 1990. The hourly ionosonde $h_m F_2$ observations in the top plot are shown as blue squares. The expected diurnal behavior of $h_m F_2$ for a site located in the southern hemisphere is clearly seen as the southward (poleward) winds drive down the layer height during the day and the northward (equatorward) winds drive up the layer height during the night. Note that balance heights for zero winds are typically approximately 50 km higher at midnight than at noon. The FLIP model fit to the observations is shown as the black line, and the climatological $h_m F_2$ from the International Reference Model (IRI) [Bilitza *et al.*, 1993, 2011] is shown as the dashed gray line. The well-known ‘midnight collapse’ of $h_m F_2$ can

be seen on most nights as the sharp downward deviations from the IRI h_mF_2 around midnight. The IRI model does a very good job of specifying the diurnal layer heights, but it does not reproduce the hourly variability of the observations. The FLIP model, however, does a very good job of reproducing both the diurnal trend and hourly variability of the h_mF_2 observations.

The lower plot of Figure 2.2 shows the magnetic meridional neutral winds determined from the h_mF_2 observations (solid black line) and the MENTAT empirical equivalent winds (solid brown line). Also shown are modeled equivalent winds using the IRI h_mF_2 in the FLIP model (gray dashed line), and the HWM14 empirical winds (stippled red line). As expected for a midlatitude station, winds are small and poleward in the daytime and large and equatorward at night.

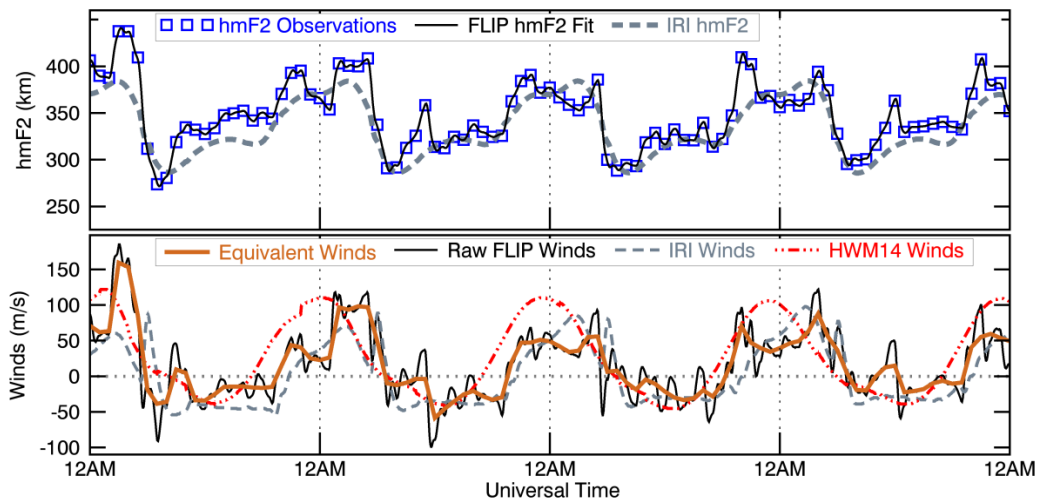


Figure 2.2. Observations and modeled values from Canberra, 1990. Top: Hourly ionosonde h_mF_2 observations (blue squares), FLIP model fit to the observed h_mF_2 (solid black line), climatological h_mF_2 from the IRI model (dashed gray line). Bottom: Raw equivalent winds (solid black line), modeled equivalent winds (solid red line), winds derived using modeled h_mF_2 from IRI (gray dashed line), and HWM14 winds (red stippled line).

The IRI-based winds exhibit the regular diurnal behavior, which is to be expected considering the regular behavior of the climatological IRI h_mF_2 values that were used to constrain the FLIP model. The HWM14 winds show the expected diurnal behavior but are nearly the same from day to day. The empirically modeled equivalent winds exhibit the timely surges and abatements that are required to move the observed h_mF_2 values up and down. The IRI-based winds and HWM14 winds, on the other hand, do not exhibit the hourly surges and abatements that are required to generate the observed h_mF_2 values. The modeled equivalent winds are the data that are used to develop the new empirical wind model.

Some of the variability in the unsmoothed equivalent winds may be real, but some variability may also be related to observational error in the observed $h_m F_2$. However, there is a peak in the wind at local sunrise in both the observed and IRI equivalent winds that is commonly seen, even when the input $h_m F_2$ is smooth. One explanation for this peak is that chemistry plays a greater role than winds in determining the location of the density peak at sunrise. This can happen when the solar EUV creates a new larger ionization peak above the existing peak. The FLIP model responds by increasing the equatorward wind to raise $h_m F_2$. Also, associated with sunrise is a rapid increase in electron temperature which generates a rapid upwelling of plasma so that there is not an equilibrium condition. Another contributing factor is related to the rapid abatement of the winds and steep decay of $h_m F_2$ around sunrise. Under these circumstances the one-hour time resolution of the measurements may not be sufficient and the IRI model may overly smooth the sunrise $h_m F_2$. Finally, the existence of two almost equal peaks could lead to ambiguity in scaling the ionograms.

CHAPTER 3: $H_M F_2$, IONOSONDE DATA, AND GEOPHYSICAL PARAMETERS

3.1 The Derivation of $h_m F_2$ Values

The derivation of $h_m F_2$ values from ionospheric characteristics is the beating heart of this research. Because of the volume of data available for constructing the empirical model; errors in $h_m F_2$ are only serious if they are systematic over many years because random errors will be averaged out in the empirical database. Nevertheless, it is important to understand the limitations of the $h_m F_2$ data.

Data from ionosondes that have been scaled by experienced operators are expected to have less than 10 km errors in height. However, the determination of key parameters by visual inspection of historical analog ionograms is susceptible to human error. Modern digisondes have automated the data scaling process but the autoscaling software has greater quality issues and human checking is often needed.

There are three principal formulations for determining $h_m F_2$ from key ionosphere parameters: (1) a simple parabolic formulation, (2) the *Dudeney* [1974, 1983] formulation, and (3) the *Bilitza et al.* [1979] formulation. The parabolic formulation was not considered for this research because it has been found by *McNamara* [2008] to have greater $h_m F_2$ errors than the *Dudeney* and *Bilitza* formulations during most of the day.

The scaled ionospheric characteristics required for determining h_mF_2 are the critical frequency of the E region [f_oE], the critical frequency of the F₂ layer [f_oF_2], and the maximum usable frequency over a distance of 3000 km divided by f_oF_2 [(M3000)F₂]. f_oF_2 and M(3000)F₂ [Shimazaki, 1955] are two of the most important characteristics scaled from ionograms. Their product, designated by MUF(3000)F₂, is the highest ordinary-mode frequency that would support a 3000 km HF communications circuit centered on the ionosonde at that time. M(3000)F₂ is variously known as the M factor, or the obliquity factor and it is used by the empirical models to evaluate h_mF_2 .

The Dudeney and Bilitza formulations use f_oE , f_oF_2 and M(3000)F₂ to estimate h_mF_2 , and each has a unique correction term to account for underlying ionization beneath the F₂ layer peak. Note that the IRI model f_oE is usually used for the calculations because the observations are often unreliable or unavailable, especially at night when the E-region density is too low to measure. E-region irregularities can also make the E-region measurement uncertain. Unlike f_oF_2 , the normal f_oE behavior can be modeled well enough that using the IRI value is reasonable. Since IRI provides an excellent monthly median estimate of the ionosphere below the F₂ peak, errors in the two formulations were determined by doing an error analysis relative to IRI model.

McNamara [2008] found that over the seven-year period from 2000 to 2006, the Dudeney formulation at midnight showed a spread of errors from ~4 km and ~26 km, reached ±10% error during the day, and the bias in the errors changed from about +15 to -5 km as solar activity decreased. The Bilitza formulation at midnight had a fixed error

spread of 40 km, the solar cycle variation of the errors during the day was less extreme than for the Dudeney formulation, and the error bias in the Dudeney formulation during the day was not seen in the Bilitza formulation, which includes a solar cycle term in its term for the underlying ionization correction factor (ΔM). Bilitza et al. is the only one using Incoherent Scatter data in addition to the ionosonde data. As noted earlier ionosonde $h_m F_2$ data have the problem of systematic errors when an e-valley is present.

Bremer [1992] found that two different formulas give essentially the same results, and then later used the Dudeney formulation for a long-term analysis of ionospheric trends (*Bremer et al* [2004]). Large, modern ionosonde databases such as Space Physics Interactive Data Resource (SPIDR) use the Dudeney formulation, and using it with the FLIP model provides a better match to the observed nighttime $N_m F_2$ than when using the Bilitza formulation. This agrees with the finding of *McNamara* [2008] that the Dudeney formulation is more accurate near midnight. Because the electron density is more sensitive to errors in ionospheric model $h_m F_2$ during the night than during the day, the Dudeney formulation has been used for this research. However, now that the data processing procedures have been developed, it would be straightforward to create a separate empirical wind model using the Bilitza formulation.

The $h_m F_2$ values for this research were calculated using the scaled ionospheric parameters in the NGDC CD-ROM data archive. The required parameters were read from the Ionospheric Working Group (IWG) files, the Dudeney $h_m F_2$ values were calculated, and then they were written to ASCII files for FLIP model ingest. Calculated

h_mF_2 values below 210 km were discarded because local chemistry severely affects the ability of the neutral winds to affect h_mF_2 at low altitudes calling for unrealistically large poleward winds to drive h_mF_2 down to lower altitudes. In addition, in summer at solar minimum the peak electron density often occurs around 170 km altitude in the F1 region, where the winds are ineffective.

3.2 Ionosonde Databases

An optimal data set for developing an empirical model should have a global distribution with good spatial, long temporal coverage, and have high-temporal resolution. This kind of coverage and variability is not available from incoherent scatter radar (ISR) or optical data sets due to their limited spatial and temporal coverage. The three available data sources, which satisfy these criteria are a CD-ROM data archive from the National Geophysical *Data* Center (NGDC), the Space Physics Interactive Data Resource (SPIDR, <http://spidr.ionosonde.net/spidr/>), and the Global Ionospheric Radio Observatory (GIRO, <http://giro.uml.edu/>). Figures 3.1 and 3.2 show the ionosonde locations for GIRO and SPIDR.



Figure 3.1. Global Ionospheric Radio Observatory (GIRO) sites map.

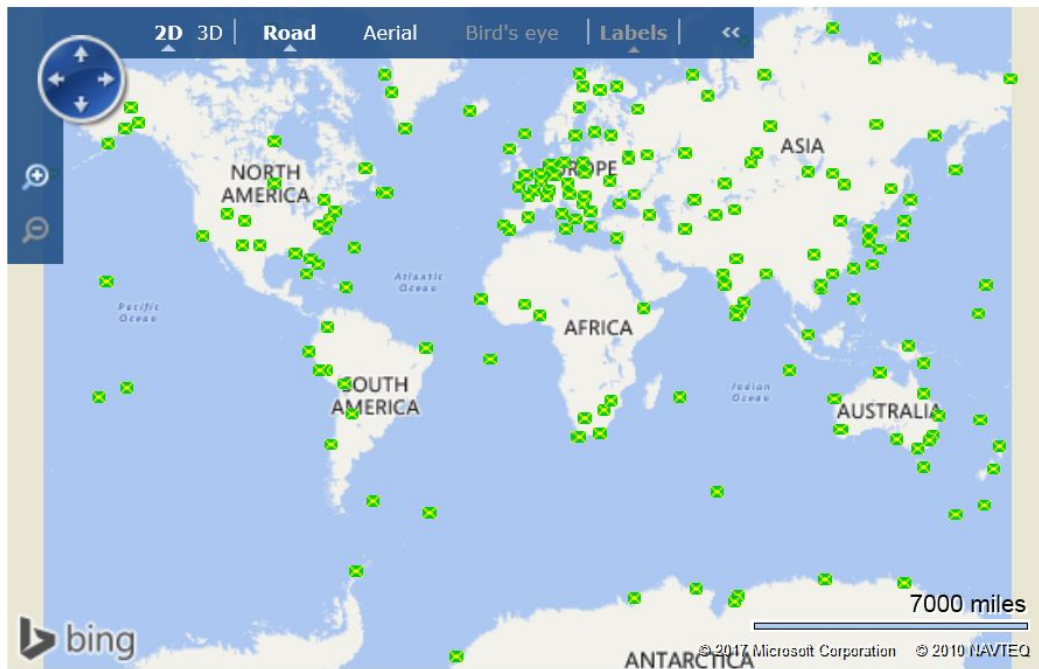


Figure 3.2. Space Physics Interactive Data Resource (SPIDR) sites map.

The NGDC dataset that was distributed on a CD-ROM was selected for this study because it is considered to be high quality, has a good global distribution, and many sites at magnetic mid-latitudes. The database, which contains hand-scaled ionosonde data at 135 sites from 1961 to 1990, spans multiple solar cycles and a large range of geophysical conditions. Furthermore, most of the individual sites have very long periods of good data. The 30-year span and 1-hour time resolution of the data allow for the investigation of thermospheric wind behavior on many different time scales. However, hand-scaled ionospheric data also have uncertainties. For example, a manual scaler must take a complex ionogram, recognize and identify its features, and develop a consistent interpretation of each one. Ideally, if multiple individuals were to independently analyze the same ionogram, the resulting scaled ionospheric parameters would be the same. Unfortunately, due to human inconsistency and the complexity of ionograms, the hand-scaled parameters can vary from one person to another.

Both the SPIDR and GIRO databases contain autoscaled data from digisondes and dynasondes, which are both upgrades of the older ionosondes and designed to make use of modern technology. They were designed to be set up and then left alone. They automatically generate multi-parameter ionospheric characteristics from the raw observations and then transmit the products to users over networks. However, digisondes often show unusual behavior. Figure 3.3 which shows coincident f_oF_2 data sets from a standard digisonde and a state-of-the-art dynasonde known as a Vertical Incidence Pulsed Ionospheric Radar (VIPR). Data from both instruments are archived at

an NGDC server and there is very good coverage throughout 2014 at Wallops Island (37.9°N, 75.5°W). Observations from the two instruments were acquired at the same dates and times, and every pair of observations differed by no more than eight seconds. The data were analyzed and 15-day seasonal medians of f_oF_2 were generated, centered on March 20 (spring), June 22 (summer), September 23 (fall), and December 22 (winter). The dynasonde medians are shown as the black circles and the digisonde medians are shown as the orange triangles. The VPIR used the PoLynomial Analysis program (POLAN) version 1.09, and the digisonde used the ARTIST-5 ionogram autoscaling software, version 0702.

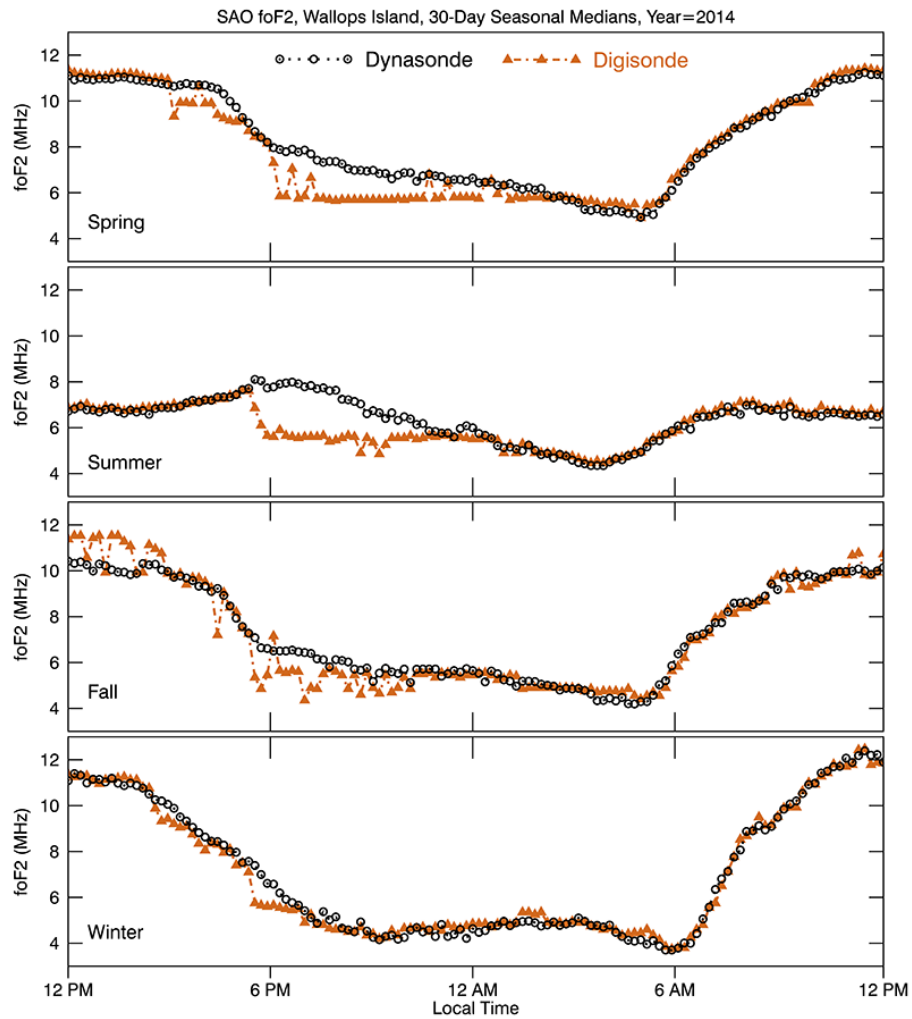


Figure 3.3. 15-day seasonal median f_oF_2 values during 2014 from a digisonde and dynasonde (VIPR) co-located at Wallops Island. The observations from each instrument are coincident within eight seconds.

Figure 3.4 shows that the median dynasonde f_oF_2 values are regular and behave as expected. However, the monthly median digisonde f_oF_2 values are unexpectedly low between 6:00 PM and midnight in every season, low values during the late afternoon in the spring, and high values in the early afternoon in the fall. Once again, the two

instrument curves differ significantly from approximately the late afternoon to around midnight. The blue dashed line shows h_mF_2 from the IRI model, which is based on old ionosonde data. The green shaded regions on each plot represent the difference in altitude between the median h_mF_2 values at each time (see the right axes). The ionospheric scale height is approximately 45-50 km around h_mF_2 , so a horizontal dotted line is drawn from the right axes to indicate where the differences approach or exceed 50 km. The differences in h_mF_2 between the digisonde and dynasonde data reach or exceed 50 km in the spring, summer and fall seasons. It should be noted that there are no specific, contextual data quality flags that describe why any of the digisonde data may be low. Bad data values in the Standard Archiving Output (SAO) files are simply indicated with the value '9999'.

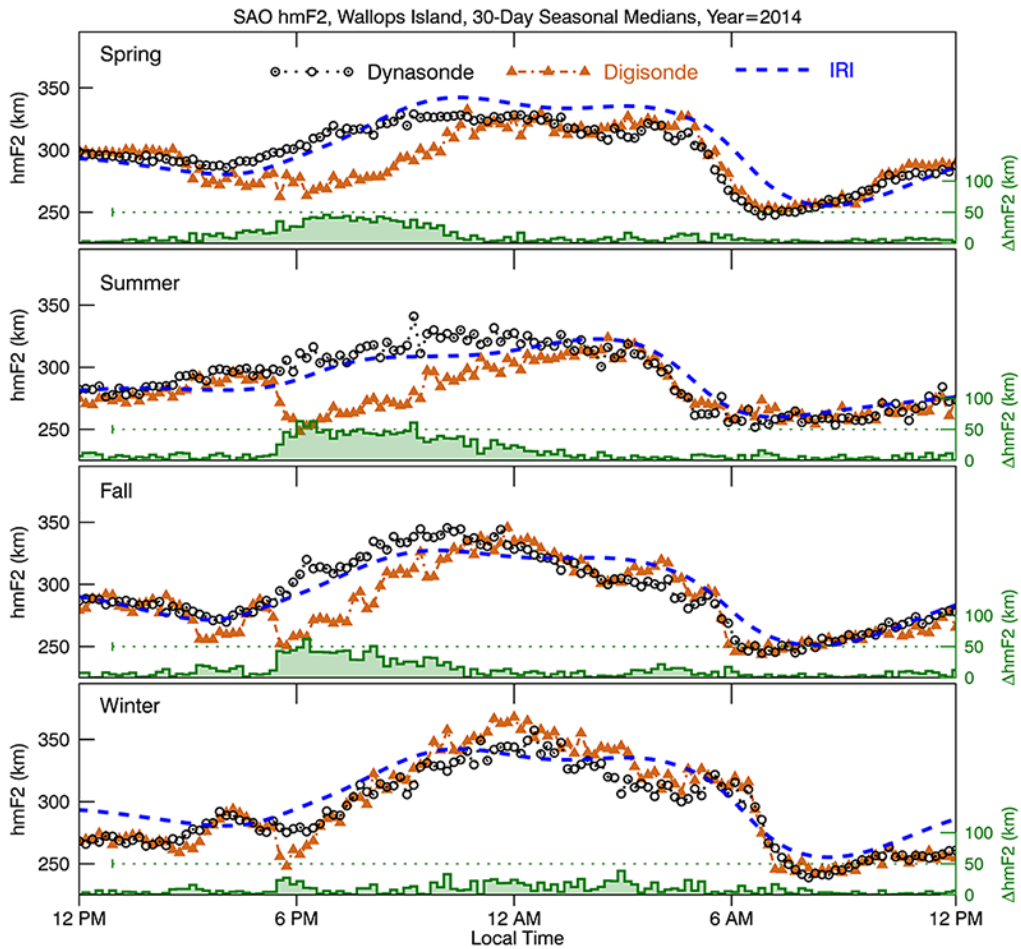


Figure 3.4. 15-day seasonal median h_mF_2 values from the sites in Figure 3.3. IRI h_mF_2 is the dashed blue line. The dotted green line at 50 km represents the approximate ionospheric scale height at h_mF_2 , and the green shaded area is the difference between coincident digisonde and dynasonde h_mF_2 values.

The SPIDR data archive ranges from the early 1940s to the current date and spans multiple solar cycles. It contains the NGDC CD-ROM data as well as more recent hand-scaled ionosonde and autoscaled digisonde data. However, there are significant gaps in the SPIDR database. Figure 3.5 shows the number of stations in the SPIDR database as a function of time. The amount of data increases sharply just before 1960

but then decreases sharply for about 5 years. It picks up again until the early 1970s when it drops by nearly 90% for a few months. The number of sites recovers, but then decreases steadily until modern times and includes three long periods with significant data dropouts in the 1990s.

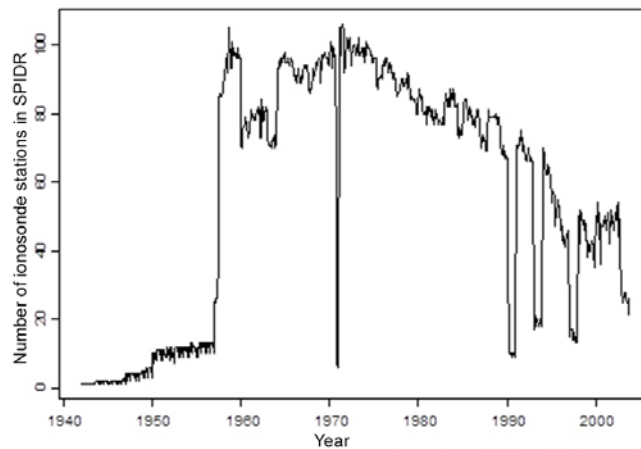


Figure 3.5. Number of stations vs. year in the SPIDR database.

Another issue with the SPIDR system relates to data provenance. The SPIDR database uses database ‘mirroring’ which defines a principal (or primary) server instance to provide (mirror) the contents of the *database* to each of the remote client database instances. The principal server for SPIDR is in Boulder, so its contents are the ‘reference data’ which are pushed to all the other servers. Figure 3.6 shows a month of f_oF_2 data at Hobart, hosted in two separate copies of the SPIDR database. The original f_oF_2 observations were scaled and stored in the Ionospheric Prediction Service (IPS) database in Australia. Those data are shown in the lower plot of Figure 3.6. The upper

plot of Figure 3.6 shows the mirrored version as displayed in the main SPIDR database in Boulder. Clearly, the Hobart f_oF_2 data are corrupted at Boulder because some of the f_oF_2 data are missing and some of the magnitudes are changed.

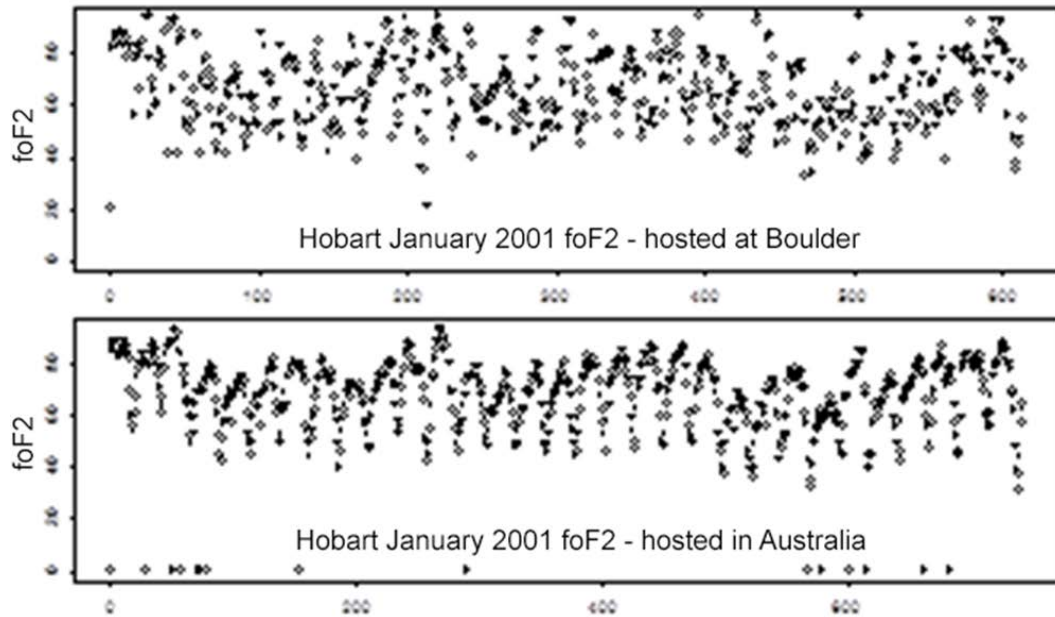


Figure 3.6. Example of SPIDR data corruption. Top: Hobart f_oF_2 data from January 2001, hosted in the Boulder SPIDR database. Bottom: The same data set, hosted in the Australian SPIDR database (before being corrupted by Boulder).

The GIRO database currently contains modern bottomside sounder (digisonde) autoscaled data from 1987 to 2017. However, Table 3.1 shows that the number of instruments during those 20 years varies significantly, increasing gradually from one site in 1987 to eight in 1998, to 52 sites in 2017. Half of the GIRO sites are in the high- and low-latitude regions and therefore not useful for the equivalent winds database.

Table 3.1. History of the ionosonde sites in the GIRO database.

Year	# of instruments
1987	1
1992	2
1997	8
2002	14
2007	33
2012	36
2017	52

There is a large database of high-quality hand-scaled data available from the Australian Ionospheric Prediction Service from the 1990s and 2000s independent of SPIDR. These data have not been included for this dissertation because matching high-quality data are not available from the other stations. This and other validated data can be incorporated in later versions of MENTAT.

3.3 Geophysical Parameters

The NGDC database spans from January 1, 1961 to December 31, 1990, a period that starts close to the end of solar cycle 19 and ends near the peak of solar cycle 22. The solar radio flux at 10.7 cm, known as the F10.7 Index, is a long-used indicator of solar activity. It correlates well with the solar sunspot number and ultraviolet (UV) solar irradiance data. Figures 3.7(a) and 3.7(b) show the daily F10.7 and the 81-day average F10.7 (F10.7A) indices, respectively, for each decade of data. The F10.7 values range from 65 to 375 and the F10.7A values range from 68 to 230. It can be seen from the F10.7A data that the solar flux was highest during the 1981 to 1990 decade (green line), except for years 6 and 7 when the first decade dominated (red line). Figure 3.7(c) shows

the yearly mean total sunspot number (SSN) for the years 1700 to 2016. The years of data used in this research are represented by the shaded yellow region. It can be seen from the plot that the time span of the NGDC data archive includes historically powerful solar maxima.

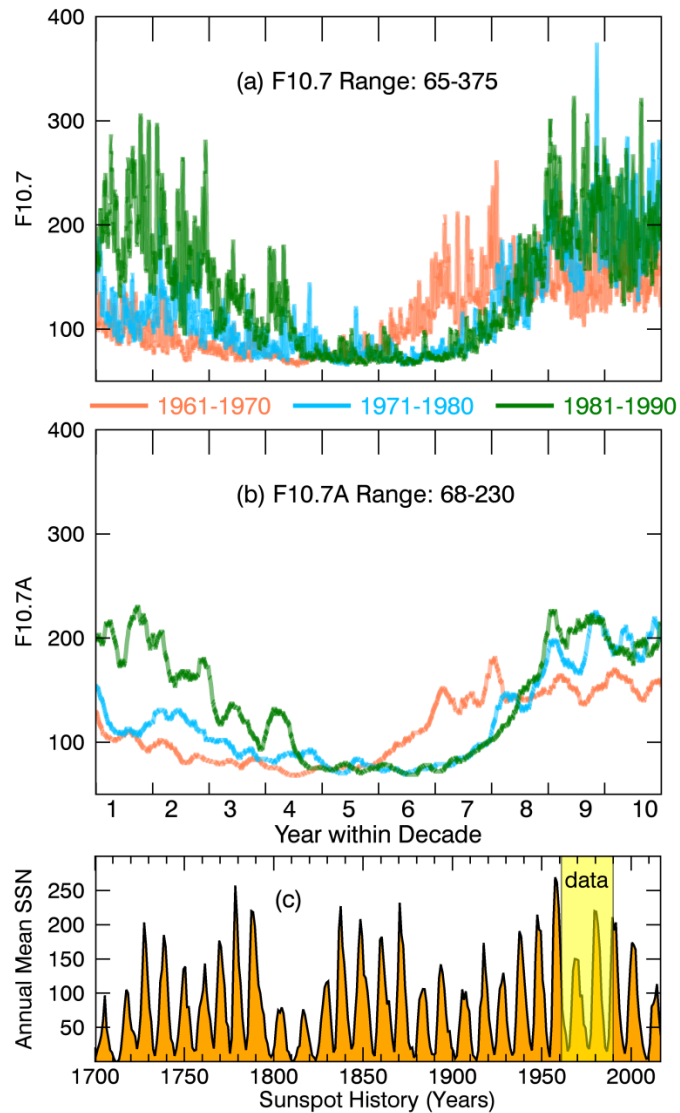


Figure 3.7. (a) F10.7 and (b) F10.7A solar flux indices during the three decades used in this study. (c) Yearly mean total sunspot number from 1700 to 2016. The three decades of data used in this research are represented by the shaded yellow region. [SSN data courtesy of SILSO data/image, Royal Observatory of Belgium, Brussels.]

Histograms of the 3-hour Kp, F10.7, and F10.7A indices are shown in Figure 3.8. Over the 30-year period, the Kp indices had a mean of 2.2, a median of 2.0, and a standard deviation of 1.4; the F10.7A had a mean of 123, a median value of 108, and a

standard deviation of 49; the F10.7A had a mean of 123, a median of 110, and standard deviation of 45. The Kp values spanned its full range from 0 to 9, but both the mean and median values are well within the range of ‘quiet time’ values. The mean, median, and standard deviation values for the F10.7 and F10.7A indices are nearly identical, but the 81-day averaging results in a significantly different range and distribution for F10.7A.

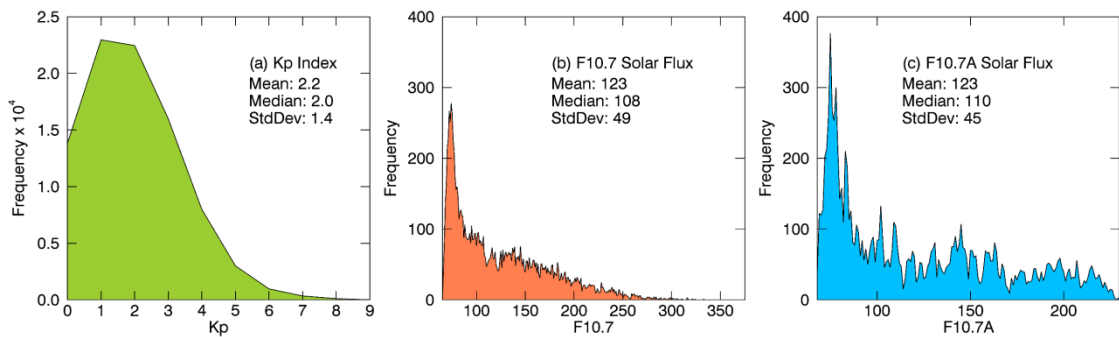


Figure 3.8. Distribution of the (a) 3-hour planetary Kp geomagnetic index, (b) F10.7 solar flux index, and (c) F10.7A solar flux index during the three decades used in this research.

This is emphasized by the box-and-whisker plots for the Kp, F10.7 and F10.7A that are provided in Figure 3.9. These plots clearly show the low median values, relatively narrow distributions, and difference between the two solar flux ranges.

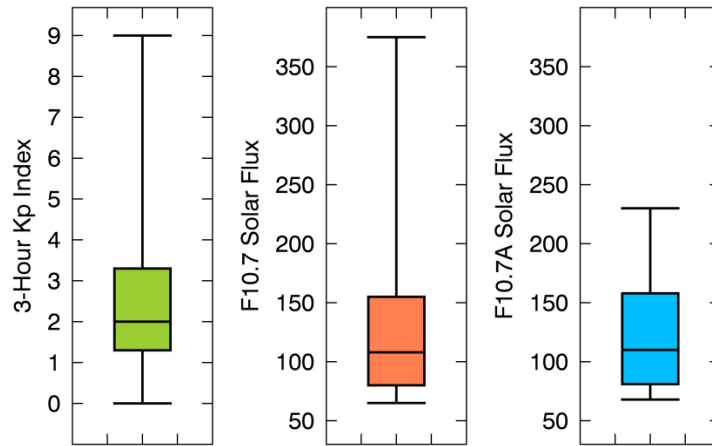


Figure 3.9. Box-and-whisker plots for the (a) 3-hour Kp Index, (b) F10.7 solar flux, and (c) F10.7A solar flux values during the three decades used in this research.

CHAPTER 4: MODELED WINDS AND VALIDATION

4.1 Background

This chapter presents a validation of the model equivalent wind technique by comparison to recent optical wind measurements. At the time of this writing, the best wind observations in the thermosphere come from optical Fabry-Perot interferometer (FPI) instruments which derive neutral wind vectors and temperatures of Earth's thermosphere using measurements of the atomic oxygen 630 nm red line emission.

There are some issues when dealing with optical wind data. First, they are only available on cloudless nights. Second, there is a mismatch in altitude because the emission peaks at an altitude approximately one scale height (~ 60 km) below $h_m F_2$ (D. Fisher, pers. comm.). The FLIP model calculates the 630 nm red line emission and it also produces an emission peak about 60 km below $h_m F_2$ for the 2014 data considered here. Because of this mismatch in altitude, the use of optical winds in ionospheric models could be problematic if there were a strong altitude dependence because all ionosphere models ideally need the winds near $h_m F_2$. Third, there is the possibility of contamination of the signal by mesospheric OH vibrational transitions at 628.7, 629.8, and 630.6 nm [Burnside *et al.*, 1990; Mende *et al.*, 1993]. If the OH contamination is an isotropic signal, there will be a small effect on the horizontal winds, amounting to roughly half the effect

seen in the vertical winds. We can apply this knowledge of the measured vertical winds to correct the horizontal measurements. We filtered out times where the magnitude of the vertical winds is greater than 10 m/s, which should limit OH effects in the horizontal data.

The FLIP model is well-suited to investigating the neutral winds because it combines an accurate representation of Earth's magnetic field with comprehensive photochemistry. It is very important that any model reproduces h_mF_2 values to within a few kilometers to reduce the large uncertainties in the electron density that can arise from uncertainties in the neutral wind. In fact, it is not possible to accurately model the electron density if a model does not accurately reproduce h_mF_2 values.

The capability of the FLIP model to reproduce observed ionospheric parameters has been validated extensively for more than 25 years. The FLIP model has been shown to accurately recreate observations of h_mF_2 , N_mF_2 , thermospheric temperatures and neutral densities, and equivalent magnetic meridional neutral winds during both geomagnetically quiet and storm periods [Buonsanto *et al.*, 1989, 1997; Dandenault *et al.*, 2015; Dyson *et al.*, 1997; Miller *et al.*, 1987; Richards *et al.*, 1989, 1991, 1994, 1995, 1998, 2009, 2010]. Previous studies found that the equivalent winds compared well to the FPI wind measurements. This study uses a more extensive modern data set than used previously.

4.2 Validation of Equivalent Winds with Optical Wind Observations

More than four months of recent, high-quality FPI wind and temperature data from the North American Thermosphere Ionosphere Observing Network (NATION) [Makela *et al.*, 2014] were available to validate the FLIP model equivalent winds. NATION consists of a network of three FPIs in the Midwest of the United States. The three FPI sites are located close to each other in latitude and longitude and have a similar, magnetic inclination and declination (see Table 4.1 and Figure 4.1). No high-quality ionosonde h_mF_2 observations were available close to the FPI sites, so h_mF_2 values from the IRI empirical model were used as the input to the FLIP model. This was a magnetically undisturbed period; the 3-hour geomagnetic Kp indices only exceeded 3.3 seven percent of the time during all four seasonal periods. For such quiet times, it is reasonable to use the IRI empirical model h_mF_2 values to derive the meridional equivalent winds for this study. The FPI sites are in a magnetic mid-latitude region where vertical plasma drifts are expected to be driven primarily by the meridional neutral winds with minimal contributions from electric fields.

Table 4.1. Geographic Latitude (LAT), Longitude (LON), and Magnetic Declination (BDEC) of the three Fabry-Pérot interferometers.

Site ID	Lat °N	LON °W	BDEC °W
UAO	40.2	88.2	2.9
VTI	37.2	80.4	8.3
PAR	35.2	82.8	6.2



Figure 4.1. Map showing the geographic location of the FPI sites.

Figure 4.2(a) shows the equivalent and observed winds at the three FPI sites on the night of March 23, 2014. The FPI optical integration time for each wind observation was 15 minutes. The FLIP (solid black line) and HWM14 (dashed red line) model winds are only plotted for PAR (35N, 83W) because the model differences are small. Positive winds are northward (poleward) and the winds are oriented along the local magnetic meridian. The horizontal dotted line in the wind plot denotes where the winds change direction. The VTI and PAR observations are in very good agreement but they differ significantly from the UAO winds. The difference is attributed to the presence of clouds which pull the winds towards zero. In general, the FPI winds (green squares) are northward (poleward) until 6:00PM and thereafter become southward (equatorward). There are several hours around midnight when the observed southward wind speed decreases for a few hours and then increases. This behavior is also seen in the equivalent winds at each site. The HWM14 model winds (dashed red line) are in fair agreement

with the magnitudes of the wind data but they do not exhibit the abatement of the wind speeds around midnight. Both the FPI observations and the equivalent winds change direction from northward to southward between 6:00PM and 8:00PM local solar time, but the HWM14 winds are always equatorward.

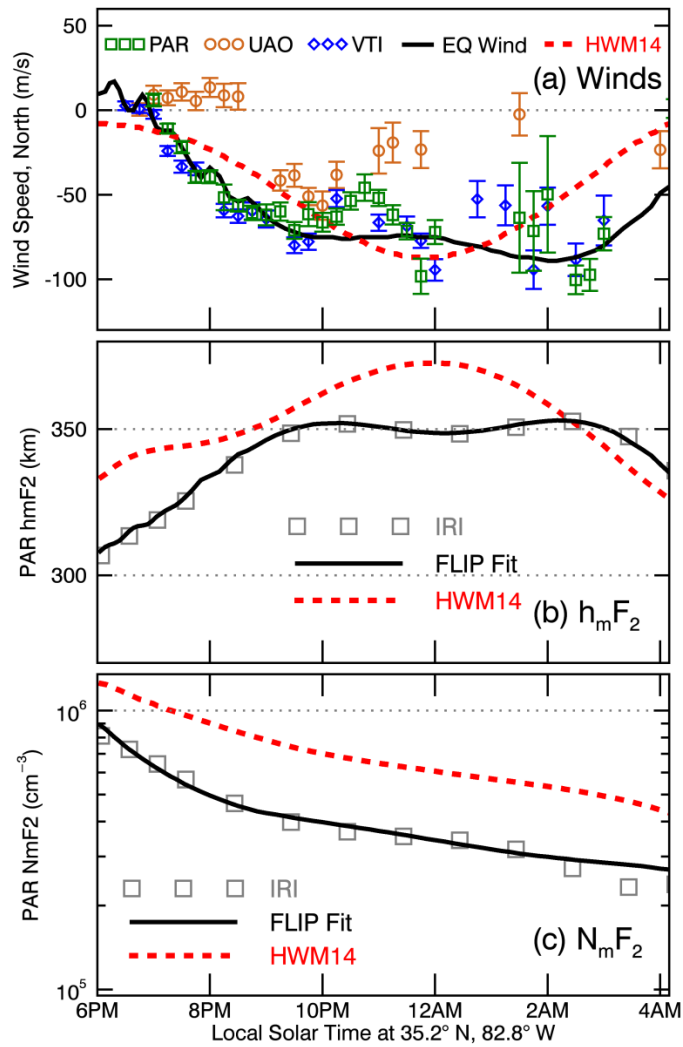


Figure 4.2. (a) Winds, (b) $h_m F_2$, and (c) $N_m F_2$ at each FPI site on March 23, 2014. Winds are oriented along local magnetic meridional. The horizontal dotted lines in (a) indicate when the winds change direction from northward to southward, or vice versa. The differences in $h_m F_2$ and $N_m F_2$ at the three sites are small, so only the values at PAR are shown.

Figure 4.2(b) and 4.2(c) show the model $h_m F_2$ and $N_m F_2$ for the same period. Only the values at PAR are shown, because the $h_m F_2$ and $N_m F_2$ curves were nearly identical at each of the three sites. Figure 4.2(b) shows the IRI $h_m F_2$ as gray squares, the FLIP fit to

the IRI values as the thin black line, and the h_mF_2 from the HWM14 winds as the dashed red line. The FLIP model does a very good job of fitting the IRI h_mF_2 . However, the FLIP model h_mF_2 from HWM14 winds is higher over the entire period. Figure 4.2(c) shows the effects of the winds on N_mF_2 . The N_mF_2 generated by using the HWM14 winds is too high over the entire period. The FLIP N_mF_2 is closer to the modeled IRI N_mF_2 values.

Differences in the neutral wind speed and direction are very important for ionospheric density modeling because the winds retard or enhance the movement of plasma along the magnetic field lines and therefore the local electron production and loss rates. In the equilibrium case with the ionosphere sunlit, the O^+ production rate rapidly exceeds the loss rate with increasing altitude in the F2 region. In the equilibrium situation, the only way most of this excess O^+ can be lost is to diffuse downwards to regions of greater N_2 and O_2 concentration (a small amount of O^+ may be converted to H^+ in the topside and finds its way into the plasmasphere). Poleward winds decrease N_mF_2 by enhancing the downward flow to regions of higher loss rates. At night, the equatorward neutral wind acts to preserve N_mF_2 by retarding the downward motion of the O^+ to regions of greater loss rate.

It is a common misconception that equatorward winds increase N_mF_2 by pushing O^+ up the field lines. This may happen briefly when the wind speed changes rapidly. For the calculations presented here, the FLIP model produces downwards fluxes below ~ 450 km at all local times, except at sunrise when large increases in electron temperature cause a strong O^+ outflow independent of the wind direction. The sunrise

temperature enhancement is well known and extensively studied [Stolle *et al.*, 2011]. The predominantly downward directed O^+ flow below ~ 450 km has been known since the mid-1960s from the Millstone Hill radar O^+ velocity measurements of Evans [1975]. The FLIP to IRI model $N_m F_2$ ratio is close to unity during the entire day when using the IRI $h_m F_2$ as the wind proxy during this period. The good agreement of the FLIP and IRI model $N_m F_2$ validates its use for this study. Using the HWM14 model causes the FLIP model to overestimate the nighttime densities because of the higher $h_m F_2$ in the evening.

The northward equivalent winds near 6:00 PM enhance the modeled plasma downward flow reducing $N_m F_2$, whereas the oppositely directed HWM14 winds retard the downward flow and enhance $N_m F_2$. Similarly, the abatement of the southward equivalent winds and FPI winds between 10:00 PM and 2:30 AM would slow the rate of $h_m F_2$ increase and cause $N_m F_2$ to decay more quickly. The HWM14 winds do not exhibit this temporary decrease in the southward wind speed between 10:00 PM and 2:30 AM, so $h_m F_2$ is higher and the local modeled loss rate during this period would be lower than that calculated from the FPI or equivalent winds. These wind dynamics are critical for specific modeling studies such as the $h_m F_2$ midnight collapse phenomena [Nelson and Cogger, 1971; Behnke and Harper, 1973; Harper, 1979; Cray and Forbes, 1986; MacPherson *et al.*, 1998; Seker *et al.*, 2009; Vlasov *et al.*, 2005; Dandenault *et al.*, 2015] and the local variations in thermospheric temperature and density near midnight [Akmaev *et al.*, 2009; Akmaev *et al.*, 2010; Ruan *et al.*, 2014].

The FLIP model depends on the accuracy of the NRLMSISE-00 model neutral atmosphere, which has been shown to reproduce average satellite drag and mass spectrometer data to within ~15% during magnetically quiet times, and comparisons with measurements indicate that the modeled atomic oxygen density is very reliable near $h_m F_2$ altitudes (see discussion by *Richards et al.* [2010]). Figure 4.3 shows there is very good agreement between the PAR and VTI observed and NRLMSISE-00 neutral temperatures but the UAO temperatures are much higher. This temperature difference mirrors the wind differences between the three sites. Figure 4.3 also shows the FLIP model ion, and electron temperatures for PAR. The model temperatures are for an altitude of 276 km to match the 630 nm peak emission altitude, but there is little vertical temperature gradient above ~270 km. The FLIP model ion temperature is just a few degrees higher than the NRLMSISE-00 neutral temperature because of the tight coupling between the ions and neutrals at this altitude. The electron temperature is higher than the neutral temperature in the early evening because of residual heat flow from the plasmasphere, but it quickly approaches the neutral temperature after sunset. The PAR and model temperatures decrease throughout the night. The VTI and UAO temperatures also decrease until about 2 am.

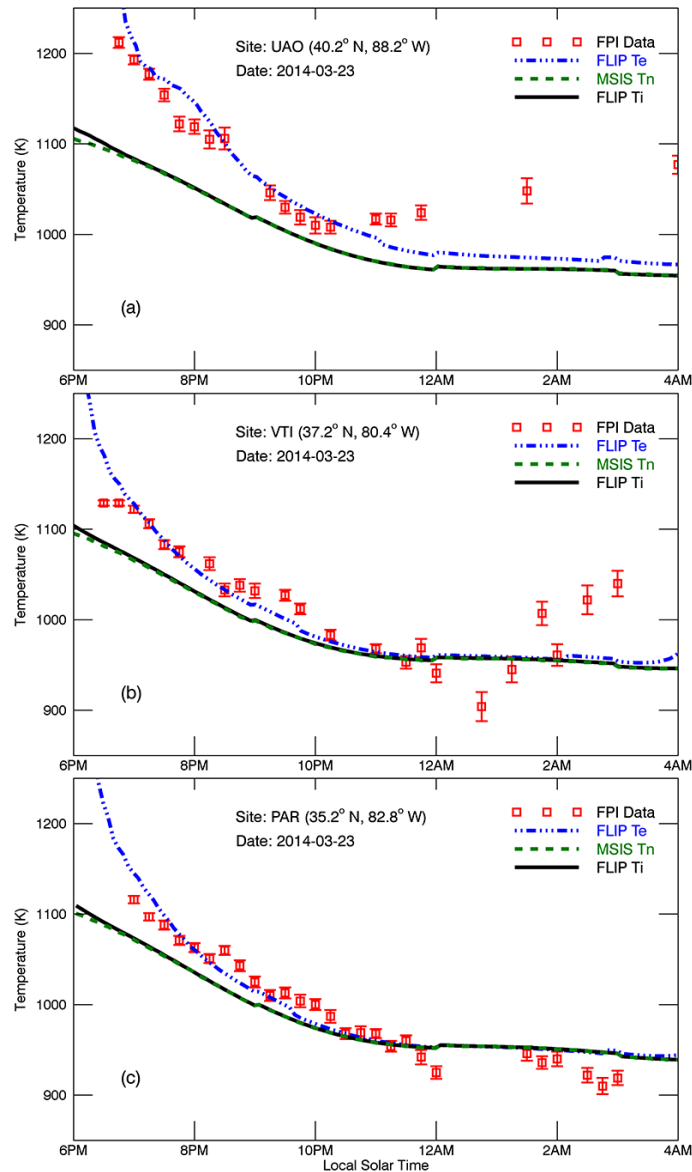


Figure 4.3. Thermospheric ion and electron temperatures from the FPI observations, FLIP model, and NRLMSISE-00 model for the same dates and times as Figure 4.2.

4.3 Seasonal Comparisons

Figure 4.4 shows the nighttime winds and their medians at the PAR site during the four seasons in 2014. The PAR instrument was chosen for this comparison because it

had the most wind observations overall and the most wind observations in each 15-minute time interval. The spring period consists of 25 days of data, spanning March 22 to April 15 UT, 2014. The summer period consists of 29 days of data, spanning June 16 to July 14. The fall period consists of 30 days of data, spanning October 17 to November 15. The winter period consists of 31 days of data, spanning January 19 to February 18.

For each season in Figure 4.4, the black dots with red error bars in the top frame show all the 15-minute FPI observations while the solid black lines show the median winds for each season. The center frames display the modeled equivalent winds for the spring period with overlapping green lines while their medians are shown as the dashed black line. The lower frames, compare the medians of the FPI (solid black) and equivalent (dashed black) winds with the HWM14 model (blue lines) winds. The median HWM14 winds are shown as the black stippled lines.

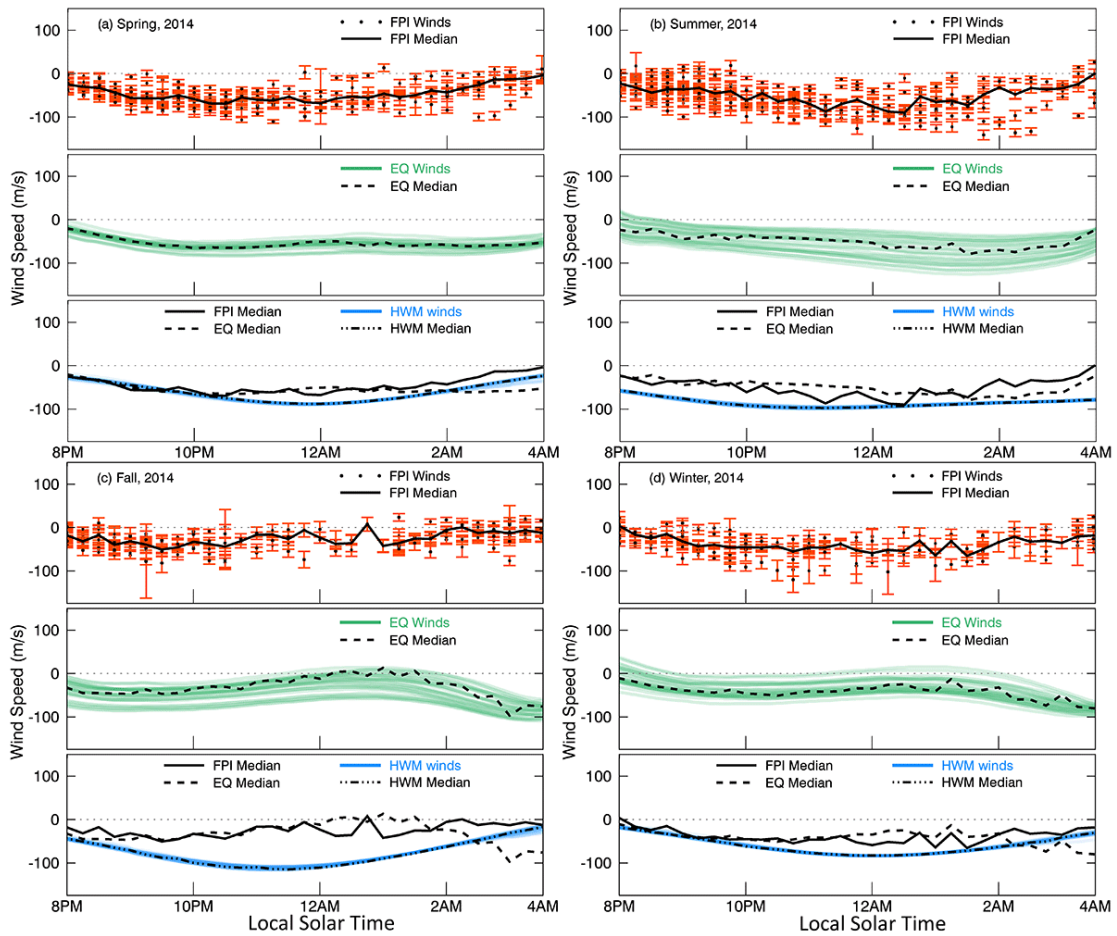


Figure 4.4. Observed and modeled seasonal (a, b, c, d) magnetic meridional neutral winds at PAR in 2014. FPI wind observations with red error bars are shown in the top panes. Modeled equivalent (EQ) winds are shown in green in the center panes. Modeled HWM14 winds are shown in blue in the lower panes. Seasonal FPI and EQ medians are shown as black lines. The FPI and EQ medians are repeated in the lower panes for comparison with HWM14.

Between 8:00 PM and 2:00 AM, the median equivalent winds track the hourly variations of the observed winds closely and better than the HWM14 winds, especially in the fall. However, between 2:00 AM and 4:00 AM in the spring, fall, and winter periods, the equivalent wind speeds remain steady or increase southward in contrast to

the observed and HWM14 winds. The steady equivalent winds after 2:00 AM in the spring period occur because the median IRI $h_m F_2$ values remain steady at those local times. The increasing southward equivalent winds after 2:00 AM in the fall and winter periods occur because the median IRI $h_m F_2$ values increase at those local times. If the $h_m F_2$ is increasing, the equivalent winds must be increasing southward.

Another important feature of the Figure 4.4 plots is the daily variability of the observations and model values. The daily variability of the equivalent winds within each season, shown by the spread in the individual green lines, is similar to the daily variability of the FPI observations, shown by the spread of the black dots and red error bars. However, the HWM14 winds exhibit little daily or seasonal variability. The equivalent wind variability must be due to magnetic activity induced changes in the neutral densities because the IRI model has little variability over one month. The strongest HWM14 winds occur around midnight in the spring and winter, and then shift to around 11:00 PM in the summer and fall. When compared to the FPI winds, they perform best in the spring period and worst in the fall period, and they differ from the FPI winds by a minimum of 35 m/s near midnight in the spring and a maximum of 100 m/s in the fall. Some of the low variability in the HWM14 winds may be explained by a low time-resolution of the wind data used by the model in this region and the empirical formulation used by the HWM models.

The results in Figures 4.2 and 4.4 suggest that the equivalent meridional neutral winds derived from the IRI model represent the FPI meridional neutral winds much

better than the modeled HWM14 winds. The larger daily and seasonal variability in the equivalent winds also suggests that they should be more physically realistic than the HWM14 winds as a function of time and geophysical conditions.

CHAPTER 5: APPLIED RESEARCH

5.1 The Midnight Collapse at Townsville, Australia

The “midnight collapse” of the ionosphere is one of the most regular and interesting dynamical features of the low-midlatitude ionosphere. It was initially observed at Arecibo, Puerto Rico and is characterized by a rapid decrease of h_mF_2 around midnight, which may be accompanied by a decrease, maintenance, or increase of the associated N_mF_2 .

Dandenault and Richards [2015] used h_mF_2 observations at Townsville to investigate the local midnight h_mF_2 morphology and to determine the local magnetic meridional neutral winds during the equinox periods of years between 1970 to 1980. Although Townsville, Australia is in the opposite hemisphere to Arecibo it has similar geographic (18.3° N, 19.6° S) and geomagnetic (30.0° N, 28.4° S) latitudes. The Arecibo data are severely limited because they are radar observations, while there is a large ionosonde database from Townsville that can be used to gain increased understanding of the midnight collapse, which is currently understood to be controlled primarily by the neutral winds.

In previous studies, the midnight collapse was attributed to changes in the neutral winds, although the role of electric fields was not ruled out. As early as 1969, the

effect of the meridional wind was shown to be stronger than that of the electric field (\vec{E}) for modifying the vertical profile of the F region ionosphere [Vasseur, 1969]. The midnight collapse at Arecibo is most likely due to neutral winds because Behnke and Harper [1973] found that the Arecibo \vec{E} field was small near midnight at equinox. The \vec{E} field contributions to h_mF_2 around midnight during equinox periods were also investigated and discounted by Crary and Forbes [1986]. Using the extensive Townsville database, Dandenault and Richards [2015] provided additional evidence that electric fields are not important for the midnight collapse by innovatively comparing equivalent winds at Townsville and a conjugate station in the northern hemisphere (Akita, Japan). If electric fields were important, the equivalent winds behavior would have been correlated because electric fields are transferred along field lines between hemispheres. However, the midnight collapse does not occur at Akita, and no relationship was found between the equivalent winds at Townsville and Akita.

The Townsville study focused on days 73-87 at the March equinox and days 260-274 at the September equinox between 1970 and 1980. The eleven years used in the study extended from the solar maximum of solar cycle 20 to solar maximum of solar cycle 21. Figure 5.1 shows the three-hour geomagnetic Kp index, atomic to molecular O to N₂ density ratio, meridional winds, h_mF_2 , and N_mF_2 at Townsville during the March equinox of 1974. The hourly ionosonde observations are shown as green circles, the FLIP model fit to the observations is shown as the solid blue line, the dashed black lines are from the IRI empirical model, and the dashed red lines represent when HWM14 winds

were used to drive the FLIP model. The FLIP model uses a running mean from the same universal time on previous days to fill any data gaps, which are rare at Townsville. Only actual data points are plotted in the figures.

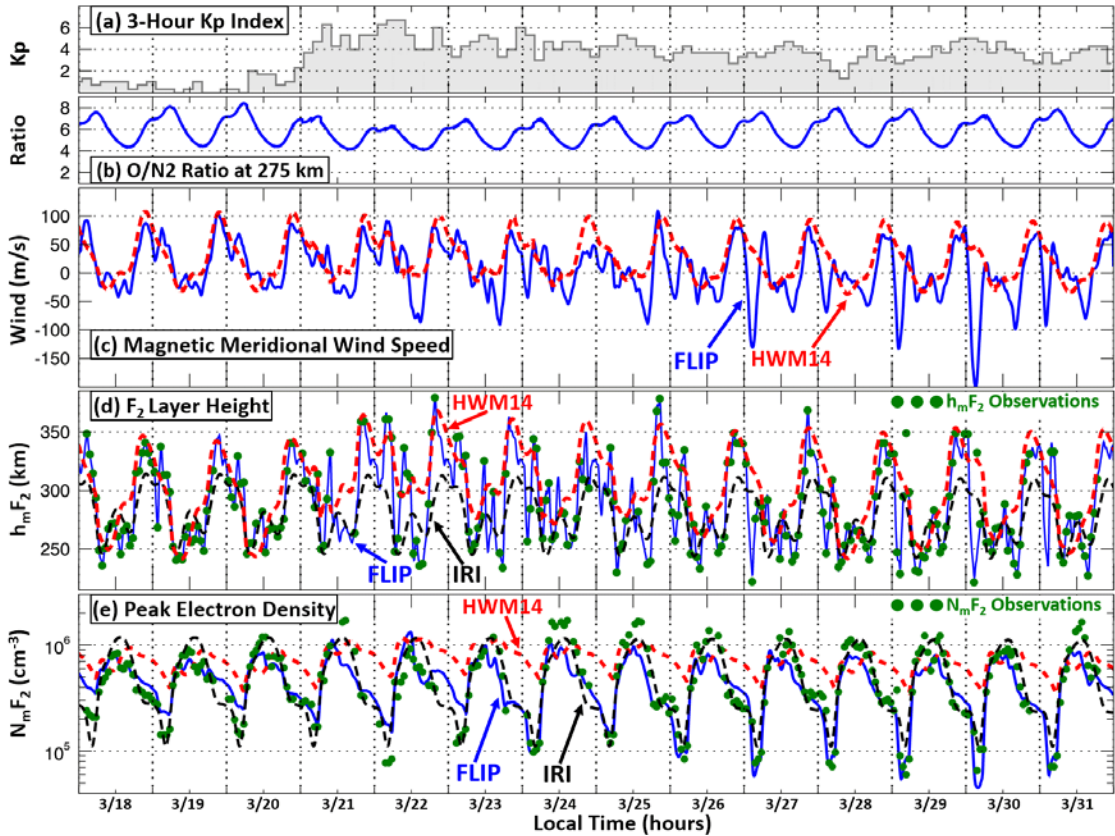


Figure 5.1. Observed and modeled data at Townsville during the 1974 spring equinox, March 18-31. (a) 3-hour geomagnetic Kp index. (b) O to N₂ ratio. (c) Modeled meridional winds, FLIP (solid blue line) and HWM14 (dashed red line). (d) Observed and modeled $h_m F_2$. Green circles are ionosonde observations, the solid blue line represents the FLIP model fit to the observations, the dashed black line represents the IRI model, and the dashed red line represents $h_m F_2$ when using HWM14 winds to drive FLIP. (e) The same as (d), but for $N_m F_2$.

The midnight collapse of $h_m F_2$ follows a regular pattern. Following a strong post sunset increase of 50-100 km, the observed $h_m F_2$ drops precipitously beginning several hours before midnight. After reaching a minimum around midnight, there is often a strong post-midnight recovery followed by the usual decay towards morning. This behavior contrasts with most mid latitude stations where $h_m F_2$ steadily increases until around midnight and then steadily decreases until morning. A clear example of the midnight collapse in the $h_m F_2$ can be seen in Figure 5.1(d) at the boundary between March 25 and 26. The midnight collapse is not seen in the IRI model which shows only a slight dip in $h_m F_2$ near midnight, or in the $h_m F_2$ when the HWM14 winds were used to drive the model. The lack of a distinct midnight collapse in the IRI model may be due to averaging in space and time because the midnight collapse does not occur at the same time every night and the station just to the south at Brisbane (28°S, 153°E) does not exhibit a distinct midnight collapse. Since there is no southward surge in the HWM14 winds before midnight, there is no downward forcing to drive a midnight collapse.

Figure 5.1(c) shows the FLIP equivalent neutral winds (solid blue lines) and HWM14 model neutral winds (dashed red lines). The equivalent winds include the required dynamics to track the $h_m F_2$ observations and to drive the midnight collapses. The HWM14 winds do not exhibit the strong poleward surge near midnight and show very little response to the geomagnetic storm that begins on May 21st. Some of the wind variation is real as shown by the later spectral analysis, but some of the rapid variation may be due to random errors in scaling $h_m F_2$. The magnetic declination is only

7° east at Townsville, which means that there is generally little contribution from the zonal winds to the magnetic meridional winds. The equivalent neutral winds are predominantly southward (poleward) during the day and predominantly northward (equatorward) during the evenings, as would be expected for a mid-latitude station in the southern hemisphere. When a midnight collapse occurs, the northward equivalent wind and $h_m F_2$ initially increase after sunset as expected, but near local midnight the wind quickly abates and may even reverse, causing the F_2 layer to descend.

The equivalent winds also lead the FLIP model to track the observed $N_m F_2$ well, as shown in Figure 5(e). Before the onset of the geomagnetic storm on March 21st, IRI does a good job of tracking the quiet time $N_m F_2$ data. During the storm, many ionosonde $h_m F_2$ observations are missing so $N_m F_2$ model-data differences increase. As the observational data become available again, FLIP again closely tracks the $N_m F_2$ data, which become very low after midnight in the week following the storm. The $N_m F_2$ generated by the HWM14 winds remains nearly the same from day to day, and does not change significantly during or after the storm period. The ability of the FLIP model to match the observed $N_m F_2$ adds confidence in the validity of the ionosonde $h_m F_2$.

5.2 Tide power spectral densities

Figure 5.2 shows the power spectral density of the major wind tides from a Fast Fourier Transform (FFT) analysis of the equivalent winds during the March (left) and September (right) equinoxes for all eleven years, 1970 to 1980. The solar cycle and seasonal characteristics of the spectral components of the neutral wind have not been

previously determined because there are insufficient wind data. This helps explain the inability of the HWM14 wind to model the Townsville $h_m F_2$. The annual mean F10.7A solar flux is shown in the March equinox plots. One striking aspect of these spectral densities is how relatively weak they all are during the years of highest solar activity. The diurnal tide varies the most with solar flux, but the semidiurnal tide becomes the most powerful wind component during some years with low solar flux (1974 to 1976). The quatradiurnal tide is also statistically significant and stronger than the terdiurnal tide during some September equinoxes. The increase in the relative power of the higher frequency components at solar minimum is consistent with the proposal that their origin is in the lower atmosphere, whereas the diurnal component is understood to be generated in situ [Jones *et al.*, 2014].

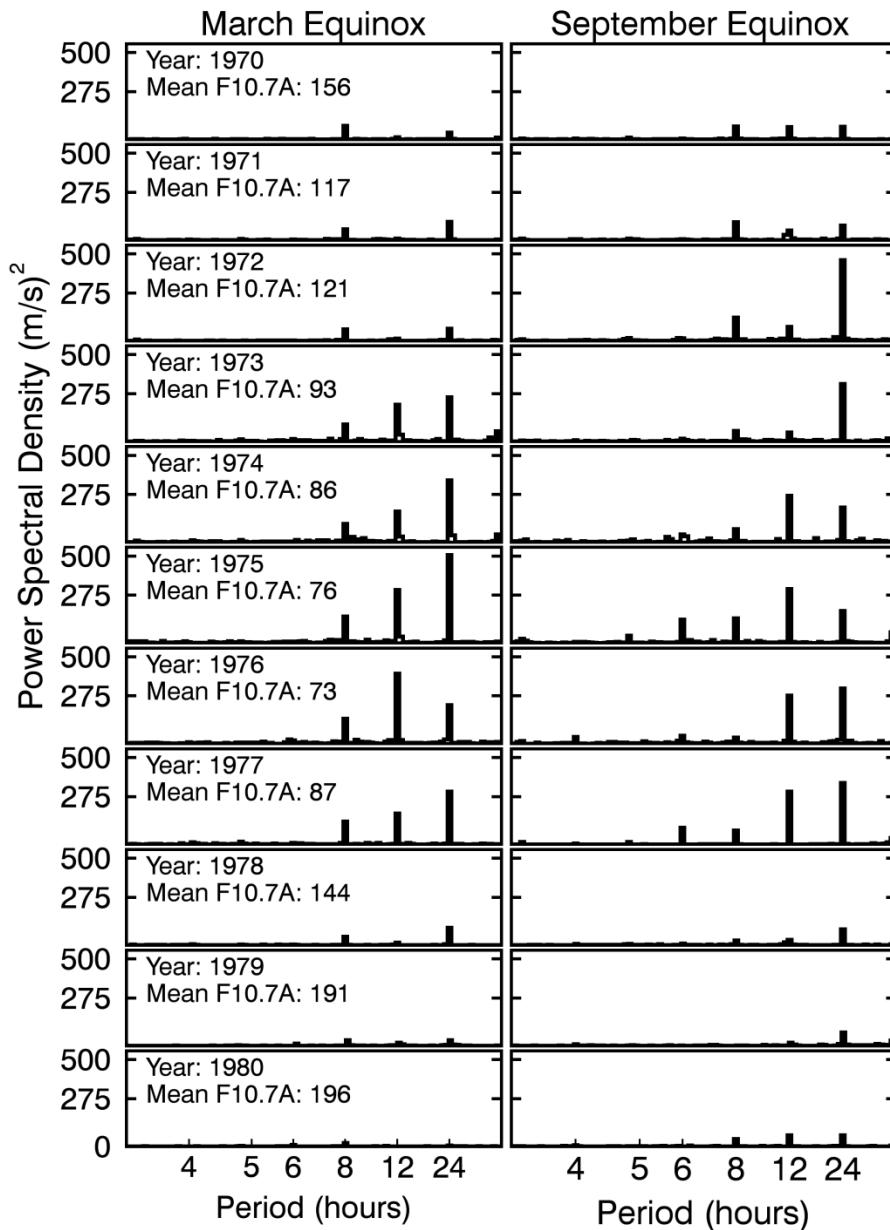


Figure 5.2. Power spectral density of the equivalent winds at Townsville for each equinox, every year from 1970 to 1980. Each data set consists of a 15-day window, centered at an equinox date. The data in the left plots were centered at the March equinox (March 20, day of year=80) and the data in the right plots are centered at the September equinox (September 23, day of year=267).

Figure 5.3 summarizes the 11-year trends of the power spectral densities from Figure 5.2. The annual mean F10.7A index is shown in the top plot of each column. The absolute strengths of the 24-, 12-, 8- and 6-hour wind components are shown on the left panel 5.3(a) and relative strengths are shown on the right 5.3(b). The general behavior of the 24-hour component power in both equinoxes is to increase as solar activity decreases, but the September equinox also exhibits a large dip from 1972 to 1977. The behavior of the 12-hour components is similar in each equinox, increasing as solar activity decreases. The 8-hour components also increase as the solar activity decreases, although not as much as the other two components, and the September component exhibits a sharp one-year decrease in 1976. The 6-hour wind component only exhibits relatively significant power in 1975 and 1977.

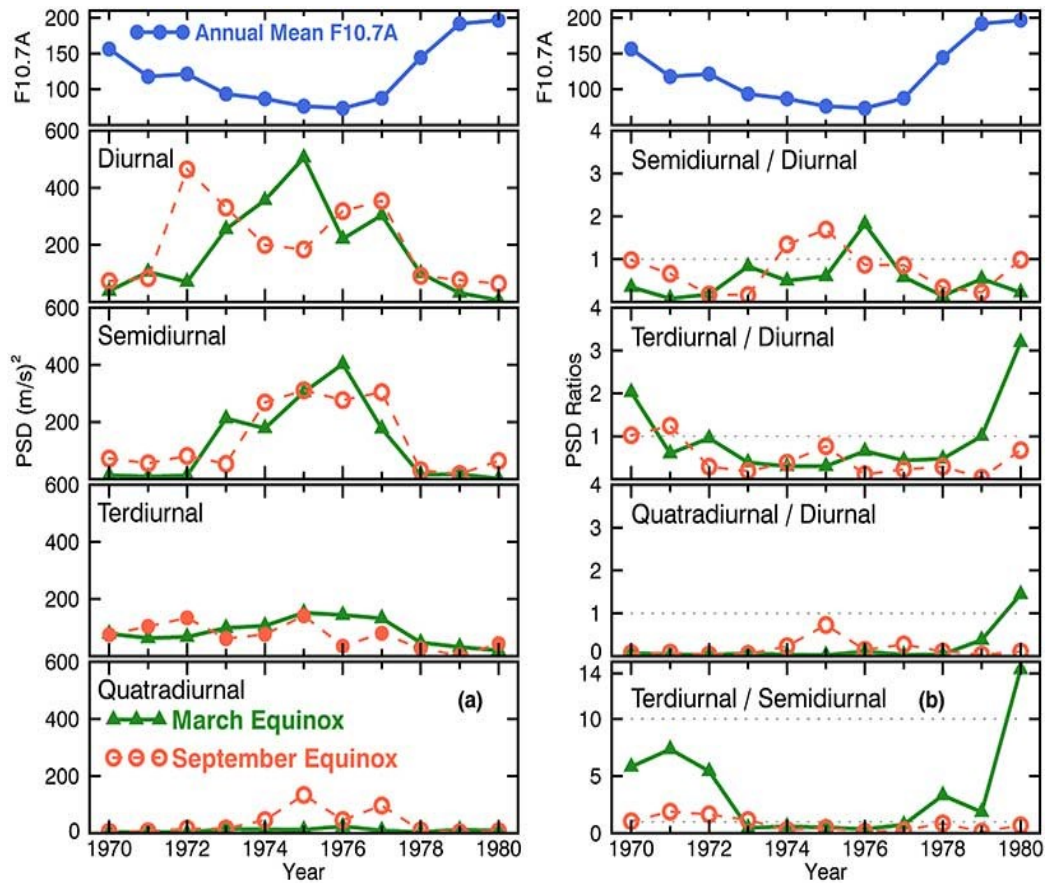


Figure 5.3. (a) March and September annual power spectral density of the diurnal, semidiurnal, terdiurnal and quadradiurnal components of the equivalent winds at Townsville (left panels). (b) March and September PSD ratios of the semidiurnal, terdiurnal and quadradiurnal components, relative to the diurnal component (right panels). The terdiurnal to semidiurnal ratio is also shown. Horizontal lines indicate ratios of 1.0 and 10.0. The annual mean F10.7A is shown at the top of each plot.

The relative power of the 12-hour, 8-hour and 6-hour wind components for each equinox is shown in Figure 5.3(b). The first three plots show the ratio of semidiurnal, terdiurnal, and quadradiurnal component power to the diurnal component power as a function of year. The bottom plot shows the ratio of the terdiurnal power to the semidiurnal power. In general, the semidiurnal/diurnal ratio in the second plot changes

inversely with the changes in solar flux. At the March equinoxes (green lines), the relative power of the 12-hour ratio increases as solar activity decreases during 1971 to 1978 and exhibits two local maxima at 1973 and 1976, reaching nearly twice the 24-hour power in 1976. In the September equinoxes (orange lines), the 12-hour ratio generally increases as the solar activity decreases during the years 1973 to 1979, and exceeds the 24-hour power by 50% and 75% in 1974 and 1975, respectively.

In contrast to the 12-hour ratios, the terdiurnal/diurnal ratios generally vary directly with the changes in solar flux. At the March equinoxes, the 8-hour wind power matches or exceeds the 24-hour wind power in 1970, 1972, 1979 and 1980. In 1970 and 1980 it has 2 to 3 times the power of the 24-hour component, respectively, and the maxima are located at the first and last years of the 11-year period, where the largest solar flux occurs. In the September equinoxes, the relative 8-hour power peaks in 1971, 1975 and 1980, but only exceeds the 24-hour power in 1971 - and then only barely.

The quatradiurnal/diurnal ratios are much lower than the other ratios. In the March equinoxes, it is relatively low until 1979, when it increases sharply for two years and exceeds the 24-hour power by nearly 50% in 1980. In the September equinoxes, it remains relatively low until the local maxima in 1975 and 1977, where it reaches levels of 75% and 30%, respectively.

The bottom plot of Figure 5.3(b) shows the ratios of the power of the terdiurnal/semidiurnal tides. In general, they both vary directly with solar flux. At the March equinoxes, this ratio becomes very large during years with strong solar flux,

exceeding values of 7 and 14 in the years 1971 and 1980, respectively. In the September equinoxes, the ratios are smaller but they are still greater than one for some years with strong solar activity.

5.3 Model determination of the origin of the midnight collapse

We ran the FLIP model with different tidal wind components to see which ones have the most influence on the midnight collapse. The equivalent neutral winds were calculated and then bandpass-filtered to isolate the important harmonics. This process generated four sets (DC+24, 12, 8, and 6 hour) that were fed into FLIP one at a time to assess their effect on h_mF_2 .

The results from the bandpass experiment are shown in Figure 5.4. Figure 5.4(a) shows the four bandpass-filtered winds and Figure 5.4(b) shows the h_mF_2 results obtained after feeding the filtered winds into the FLIP model. The midnight collapse in h_mF_2 begins to appear with the addition of the 12-hour component, but it is weak. The collapse becomes very strong after the addition of the 8-hour terdiurnal wind component. The addition of the 6-hour wind had little further effect. Calculations for other periods indicate that at different times, the 12-hour and 6-hour components may be the main influence on the h_mF_2 collapse.

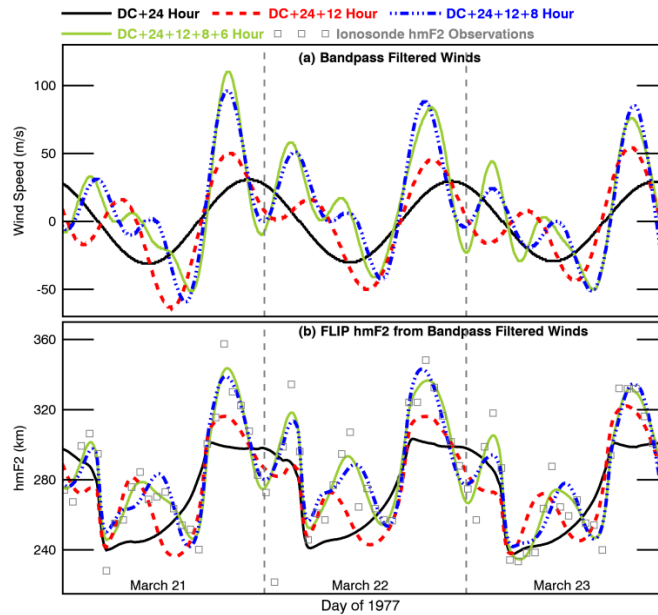


Figure 5.4. (a) Four sets of meridional winds, generated by bandpass-filtering the equivalent winds during the March 1977 equinox. The winds are obtained by successively allowing the DC component and the first four tidal components through the filter. (b) Three days of modeled h_mF_2 after using the four bandpass-filtered winds as inputs to FLIP. Squares are the h_mF_2 observations used to derive the original equivalent winds.

5.4 Conclusions from the midnight collapse analysis

Overall, the midnight collapse of h_mF_2 occurred on 89% of 330 equinox nights with a mean magnitude of 84 km in March and 99 km in September. These findings are similar to the 85% occurrence rate and 50 to 100 km collapse magnitude that were reported by *Nelson and Cogger* [1971] on a much more limited data set at Arecibo. The collapse in h_mF_2 is not with a response to increased geomagnetic activity because large nighttime decreases occur even in periods when the Kp index remains very low. In any

case, strong magnetic activity would normally produce equatorward wind enhancements, which would inhibit the descent of the F_2 layer.

Crary and Forbes [1986] proposed that higher-order (terdiurnal, quatradiurnal) components in the wind and plasma density fields are due to the interaction of underlying wind and plasma patterns. Strongly forced semidiurnal and diurnal components in the wind field and mean and diurnal components in the plasma densities (ion drag) are generated by solar irradiation. Semidiurnal modulation of ion drag due to the semidiurnal tide then feeds back to the diurnal and semidiurnal wind fields to generate the higher-order wind components. These higher-order wind components may then add temporal and vertical structure to the total wind field. The bandpass filtering experiment in our study validated the concept that the interaction of the various wind components drives the midnight collapse and that higher-order wind tides add structure to the neutral winds and $h_m F_2$.

At Townsville, the powers of the diurnal and semidiurnal components showed a strong indirect dependence on the solar activity. The terdiurnal component, however, is a regular feature and shows much less dependence on solar flux. In fact, during solar maxima, the terdiurnal component is significantly stronger than both the diurnal and semidiurnal components. Since the power of terdiurnal component is relatively independent of solar flux and dominant during solar maximum, some of its strength may be due to other factors that are regular and independent of solar activity such as zonal winds, $\vec{E} \times \vec{B}$ drift, or tidal/gravity wave interactions. The quatradiurnal wind

component is relatively weak and does not appear to be fundamental to the occurrence of a collapse, but it does contribute to the timing and slope of the wind and $h_m F_2$.

The conclusions of this research were that the midnight collapse of the equinox ionosphere is a regular characteristic of the ionospheric F_2 layer at Townsville and the rate of collapse occurrence and the average collapse magnitudes are consistent with previous findings at Arecibo. The interaction of the first three tidal components of the equivalent winds appear to be the primary driver for the midnight collapse. The diurnal and semidiurnal tides exhibit a strong indirect relationship with solar flux. The terdiurnal component exhibits a weak indirect relationship with solar flux, and becomes the most powerful wind component during solar maximum. The quatradiurnal wind component is relatively weak, but does contribute to the characteristics of the winds and underlying $h_m F_2$. The equivalent winds do a very good job of recreating the observed $h_m F_2$ and $N_m F_2$.

CHAPTER 6: EMPIRICAL MODELING

6.1 Empirical Modeling Formulation

The wind database for modeling consisted of 30 years of hourly winds at the 40 ground-based and ocean-based locations. Since the sites have a good global distribution and since the wind data are continuous in time, spatial and temporal interpolation were used to develop the new empirical wind model. The model's independent variables (input parameters) are the geographic latitude, geographic longitude, year, day of year, and universal time seconds within the day of year. These are the same input parameters used by HWM wind models, which will make this model easy to use with other models. Well-known spatial interpolation algorithms such as spline and inverse distance weighting are referred to as deterministic methods because they are directly based on the surrounding measured values or on formulas that determine the smoothness of the resulting surface. Other interpolation methods use techniques based on statistical models that include the relationships among the measured data. The generic name for the family of techniques used for mapping of surfaces from limited sample data and the estimation of values at unsampled locations is 'geostatistics'. Geostatistical methods are widely used in fields where spatial data are studied, and this is the approach that is used to estimate global meridional neutral winds where there are no modeled values.

Geostatistical estimation on a sphere (e.g., estimating the winds on Earth) is a multi-stage process. It includes exploratory statistical analysis of the data, variogram modeling, and then generating the surface. The first stage involves studying the data to establish the predictability of values from place to place in the study area. This results in a graph known as a semivariogram which models the difference between a value at one location and the value at another location according to the distance and direction between them. The next stage involves estimating values at locations which have not been sampled. This process is known as 'kriging', named in honor of Danie Krige, a well-known South African statistician and mining engineer.

Kriging uses a weighted average of neighboring samples to estimate the unknown value at a given location [Daley, 1991]. A semivariogram depicts the spatial autocorrelation of the measured sample points and, like covariance, it measures the strength of statistical correlation as a function of distance. Weights are optimized using the semivariogram model, the location of the samples, and all the relevant inter-relationships between known and unknown values. The technique also provides a "standard error" which may be used to quantify confidence levels.

Kriging [ESRI, 2017], is similar to inverse distance weighting in that it weights the surrounding measured values to derive a prediction for an unmeasured location. The general formula for both interpolators is formed as a weighted sum of the data:

$$\hat{Z}(s_o) = \sum_{i=1}^N \lambda_i Z(s_i)$$

where:

$Z(s_i)$ = the measured value at the i^{th} location,

s_i = the i^{th} location

λ_i = an unknown weight for the measured value at the i^{th} location

s_0 = the prediction location

N = the number of measured values

With inverse distance weighting, the weight, λ_i , depends solely on the distance to the prediction location. With kriging, the weights are based not only on the distance between the measured points and the prediction location, but also on the overall spatial arrangement of the measured points. To use the spatial arrangement in the weights, the spatial autocorrelation must be quantified. Thus, in ordinary kriging, the weight, λ_i , depends on a fitted model to the measured points, the distance to the prediction location, and the spatial relationships among the measured values around the prediction location.

Kriging uses the data twice: once to estimate the spatial autocorrelation of the data, and then again to make the predictions. The first step is to create variograms and covariance functions to estimate the statistical dependence (spatial autocorrelation) values that depend on the model of autocorrelation (fitting a model). The second step is to predict the unknown values.

Creating a variogram involves spatial modeling of the structure of the measured points. This begins with a graph of the empirical semivariogram, computed with the following equation for all pairs of locations separated by distance h :

$$\text{Semivariogram}(\text{distance}_h) = 0.50 * \text{mean}((\text{value}_i - \text{value}_j)^2)$$

Spatial autocorrelation simply quantifies a basic principle of geography: things that are closer together are more alike than things farther apart. Once each pair of locations is plotted after being binned, a semivariogram model is fit through them. An empirical semivariogram, shown in Figure 6.1(a), is a graph with the distance on the x-axis and the averaged semivariogram values on the y-axis. Therefore, pairs of locations that are closer together (to the far left in Figure 6.1(a)) should have more similar values (low on the y-axis). As pairs of locations become farther apart (move to the right on the x-axis), they should become more dissimilar and have a higher squared difference (move up on the y-axis).

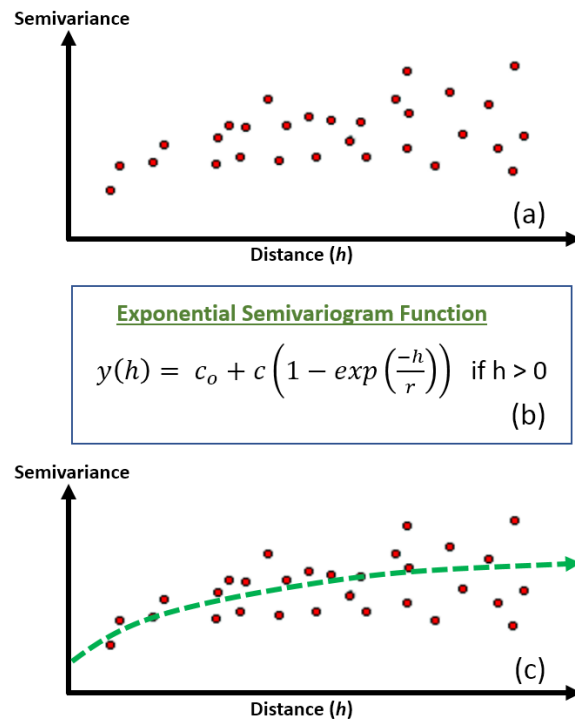


Figure 6.1. An example of a Kriging semivariogram. (a) Example of averaged semivariogram values. (b) Semivariogram exponential function for the values. (c) The values and the semivariogram function.

The next step in kriging is semivariogram modeling, which is a key step between spatial description and spatial prediction. This is done by fitting a model to the points in the empirical semivariogram plot. The empirical semivariogram provides information on the spatial autocorrelation of datasets, but it does not provide information for all possible directions and distances. For this reason, and to ensure that kriging predictions have positive kriging variances, fitting a model to the empirical semivariogram is used.

A semivariogram model consists of three parameters known as the range, sill, and nugget. The three parameters are shown graphically in Figure 6.2. The value at

which the semivariogram model attains the range (the value on the y-axis) is called the sill. The sill represents the variance of the variable. Sample locations separated by distances closer than the range are spatially autocorrelated, whereas locations farther apart than the range are not. Theoretically, at zero separation distance the semivariogram value is 0. However, at an infinitely small separation distance, the semivariogram often exhibits a nugget effect, which is a value greater than 0. For example, if the semivariogram model curve intercepts the y-axis at 2, then the nugget is 2. The nugget effect can be attributed to measurement errors or spatial sources of variation at distances smaller than the sampling interval (or both). Increasing the nugget value leads to a more equal distribution of the kriging weights and to an increase of the kriging variance. If the nugget value approaches the sill, there is no redundancy between any of the samples, and none of the samples is any closer to the point being estimated than any other in terms of statistical distance. The result is a simple average of the available data with a complete lack of spatial correlation.

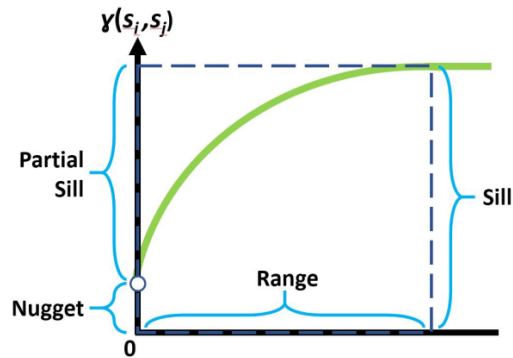


Figure 6.2. A semivariogram range, sill, and nugget.

To fit a model to the empirical semivariogram, a function is chosen to serve as the model. The function influences the prediction of the unknown values, particularly when the shape of the curve near the origin differs significantly. The steeper the curve near the origin, the more influence the closest neighbors will have on the prediction. As a result, the output surface will be less smooth. Various models are designed to fit different types of phenomena more accurately, and there are many semivariogram models from which to choose. An example of an exponential semivariogram model is shown in Figure 6.1(b) and it is plotted with the sample data in Figure 6.1(c). The exponential function fits the data well. After experimenting with various semivariogram functions, the exponential function described in Figure 6.3 was selected for use with the equivalent wind data. This form of exponential function is generally used when spatial autocorrelation decreases exponentially with increasing distance and the autocorrelation disappears completely only at an infinite distance. In practice, this

equation generated the most realistic spatial distribution of local and global wind patterns.

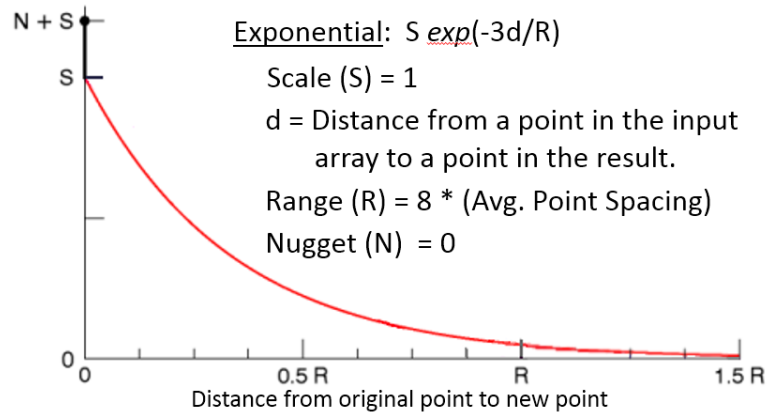


Figure 6.3. Covariance equation used for kriging the equivalent winds at the 40 ionosonde sites to a global grid. Using a symmetric 5° global grid resolution resulted in 37 latitudes and 72 longitudes.

Determining the dependence or autocorrelation in the data completes the first use of the data. The empirical semivariogram is no longer needed and we can proceed to the second step of using the fitted model to make predictions in unsampled regions. Using the kriging procedure with the exponential semivariogram model in Figure 6.3, the meridional wind speeds at the 40 mid-latitude ionosonde sites were used to estimate the global meridional wind speed using a global 5° latitude and 5° longitude grid for every hour in the winds database. The final winds database consists of 30 years of globally interpolated hourly wind data. As mentioned earlier, temporal smoothing of the meridional winds was done using range limiting, median filtering, and boxcar

smoothing. A linear interpolation is used by the model to estimate wind values between integer hours. Leap years were not accounted for, so each year of data spans 365 days (8760 hours) of time.

An example of the equivalent winds before and after interpolation to a global grid is shown in Figure 6.4. The modeled equivalent winds for UT=20 on March 25, 1990 at each of the 40 sites are shown in Figure 6.4(a), and the globally-interpolated winds for the same time are shown in Figure 6.4(b). The approximate geographic location of the subsolar point is identified by the yellow circle with the text '12PM' in its center, and the antipodal location to the subsolar point is identified by the dark gray circle with the text '12AM' in its center. As expected, the neutral winds flow away from the subsolar point (yellow circle) and toward its antipodal location (gray circle). This results in a strong flow over the poles from the dayside to the night side. The wind direction should be orientated normal to the local boundary of the magnetic mid-latitude region (light yellow shaded regions). However, the thermosphere does not react instantly to solar EUV energy deposition, so the maximum wind response may lag a few hours after the sun has reached its zenith. This effect can be seen most clearly in Figure 6.4(b), where some of the strongest wind speeds occur a few hours behind (to the right of) the geographic location of the two circles.

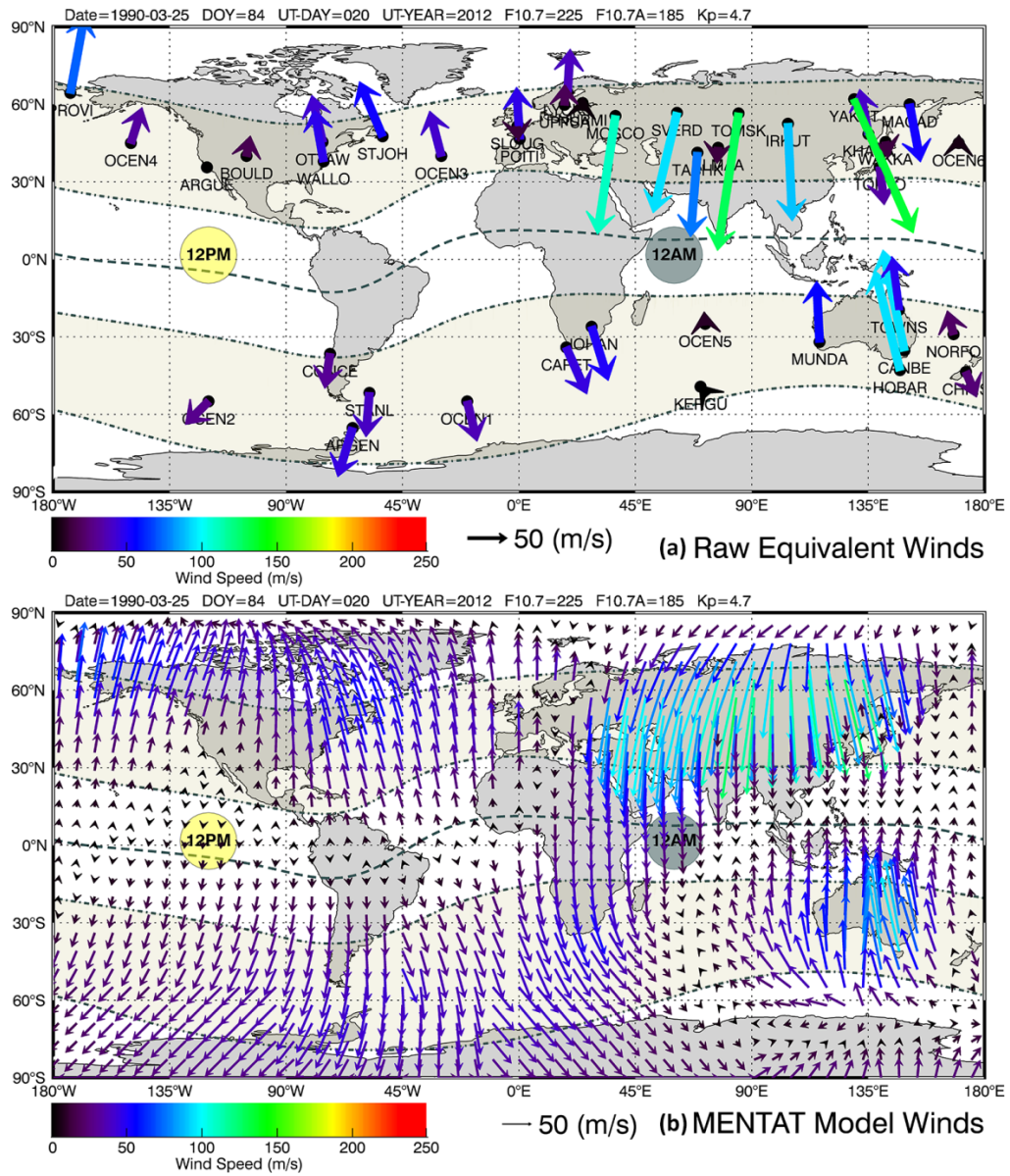


Figure 6.4. (a) Equivalent winds at each of the 40 ionosonde sites. (b) Global modeled winds map after Kriging. A 7° grid resolution was used for this map for clarity. The subsolar point is shown as the yellow circle (12PM) and its antipodal location is shown as the dark grey circle (12AM).

6.2 Global Winds Database

To develop a robust empirical model of equivalent neutral winds, global $h_m F_2$ data over long periods of time are required. However, missing or unusable values are normal in any long-term high-resolution data set. NGDC ionosonde sites in the mid-latitudes were selected that have a minimal number of gaps due to bad data. Gaps that did exist in the data were handled in variety of ways. If a gap in the data was short - on the order of hours - a running-mean based on data from the same universal time on previous days was used to replace the missing value. If a gap in the data was long - many days or weeks - FLIP was run using climatological $h_m F_2$ from the IRI model to estimate the equivalent winds for those periods. The winds based on $h_m F_2$ observations and the winds based on $h_m F_2$ from IRI were then consolidated into single, year-long wind files.

The total amount of NGDC data used for this research includes 30 years of hourly data from 34 ground-based sites in the magnetic mid-latitudes. To improve global coverage of the winds database for empirical modeling, six additional locations over the oceans were chosen. At each of these six 'ocean' sites, FLIP was run using $h_m F_2$ from the IRI model to estimate the equivalent winds for every year from 1961 to 1990. As shown previously, the diurnal behavior of IRI-based equivalent winds can be quite good - better than HWM14 meridional winds. The equivalent winds from the ocean sites were then integrated into the overall winds database so that there were 40 (34 ground + 6 ocean) sites located in the magnetic mid-latitudes with 30 years of continuous hourly wind data available for empirical modeling.

The site identifier, name, geographic location, and magnetic declination of all 40 sites are listed in Table 6.1 and a map of the sites is shown in Figure 6.5. The ground-based ionosonde sites are shown as black circles and the six ocean locations that used $h_m F_2$ from IRI are shown as blue stars. The magnetic mid-latitude regions are shown as light-yellow strips in the northern and southern hemispheres. They span the L-Shell regions from 1.2 to 5.0, which roughly translate to geomagnetic latitudes of $\pm 24^\circ$ to $\pm 63^\circ$. Most of the ground-based sites have a low magnetic declination, but a few such as Kerguelen Islands have a large magnetic declination (49.9° West) where strong zonal winds may have a non-negligible effect on the magnetic meridional wind speeds. The distribution of the $h_m F_2$ observational database from the 34 ground-based NGDC sites during 1961 to 1990 is shown in Figure 6.6. There were 5.8 million $h_m F_2$ usable observations with a minimum of 190 km, a maximum of 500 km, a mean of 299.5 km, a median of 297.2 km, and a standard deviation of 48.6 km.

Table 6.1. Location of the magnetic mid-latitude ionosondes that were used for basic research and to develop the new empirical equivalent wind model.

	<u>SITE ID</u>	<u>NAME</u>	<u>GLAT°</u>	<u>GLON°</u>	<u>BLAT°</u>	<u>BLON°</u>	<u>BDEC°</u>
01	ALMAA	ALMAATA	43.2	77.0	33.4	151.9	4.2
02	ARGEN	ARGENTINE ISL.	-65.3	295.7	-54.0	4.3	17.5
03	ARGUE	ARGUELLO	35.6	239.4	42.3	302.4	16.4
04	BOULD	BOULDER	40.0	254.7	48.9	318.2	13.7
05	CANBE	CANBERRA	-35.3	149.0	-43.7	225.7	11.7
06	CAPET	CAPETOWN	-34.1	18.3	-33.1	81.2	-22.7
07	CHRIS	CHRISTCHURCH	-43.6	172.8	-47.8	254.1	21.7
08	CONCE	CONCEPCION	-36.6	287.0	-25.3	357.7	12.1
09	HOBAR	HOBART	-42.9	147.3	-51.4	225.9	13.4
10	IRKUT	IRKUTSK	52.5	104.0	41.2	175.5	-1.7
11	JOHAN	JOHANNESBURG	-26.1	28.1	-27.2	92.8	-15.7
12	KERGU	KERGUELEN ISL.	-49.3	70.2	-57.4	129.9	-49.9
13	KHABA	KHABAROVSK	48.5	135.1	38.1	201.3	-10.7
14	LYCKS	LYCKSELE	64.6	18.8	62.5	111.8	-0.3
15	MAGAD	MAGADAN	60.0	151.0	50.9	211.6	-10.5
16	MOSCO	MOSCOW	55.5	37.3	50.7	121.5	6.6
17	MUNDA	MUNDARING	-32.0	116.2	-43.2	187.7	-4.0
18	NORFO	NORFOLK ISL.	-29.0	168.0	-34.4	244.6	14.8
19	NURMI	NURMIJARVI	60.5	24.6	57.7	113.5	2.7
20	OCEN1	OCEAN SITE 1 *	-55.0	340.0	20.6	199.1	-15.9
21	OCEN2	OCEAN SITE 2 *	-55.0	240.0	20.6	199.1	32.7
22	OCEN3	OCEAN SITE 3 *	40.0	330.0	20.6	199.1	-19.4
23	OCEN4	OCEAN SITE 4 *	45.0	210.0	20.6	199.1	21.1
24	OCEN5	OCEAN SITE 5 *	-25.0	72.0	20.6	199.1	-23.8
25	OCEN6	OCEAN SITE 6 *	45.0	170.0	20.6	199.1	3.0
26	OTTAW	OTTAWA	45.4	284.1	56.7	353.0	-12.9
27	POITI	POITIERS	46.6	0.3	49.2	83.0	-7.3
28	PROVI	PROVIDENYA	64.4	186.6	59.9	237.1	13.9
29	SLOUG	SLOUGH	51.5	359.4	54.0	84.4	-8.8
30	STANL	STANLEY	-51.7	302.2	-40.6	10.3	6.3
31	STJOH	STJOHNS	47.6	307.3	58.2	22.9	-27.4
32	SVERD	SVERDLOVSK	56.7	61.1	48.4	141.7	12.1
33	TASHK	TASHKENT	41.3	69.0	32.4	144.6	4.1
34	TOKYO	TOKYO	35.7	139.5	25.7	206.7	-6.1
35	TOMSK	TOMSK	56.5	84.9	46.0	160.6	9.0
36	TOWNS	TOWNSVILLE	-19.6	146.9	-28.4	220.5	7.8
37	UPPSA	UPPSALA	59.8	17.6	58.3	106.9	-0.8
38	WAKKA	WAKKANAI	45.4	141.7	35.5	207.3	-9.2
39	WALLO	WALLOPS ISL.	37.9	284.5	49.2	353.9	-8.6
40	YAKUT	YAKUTSK	62.0	129.6	51.2	194.9	-14.3

* Ocean-based location that used IRI hmF2 estimates as the FLIP model constraint to derive the equivalent neutral winds.

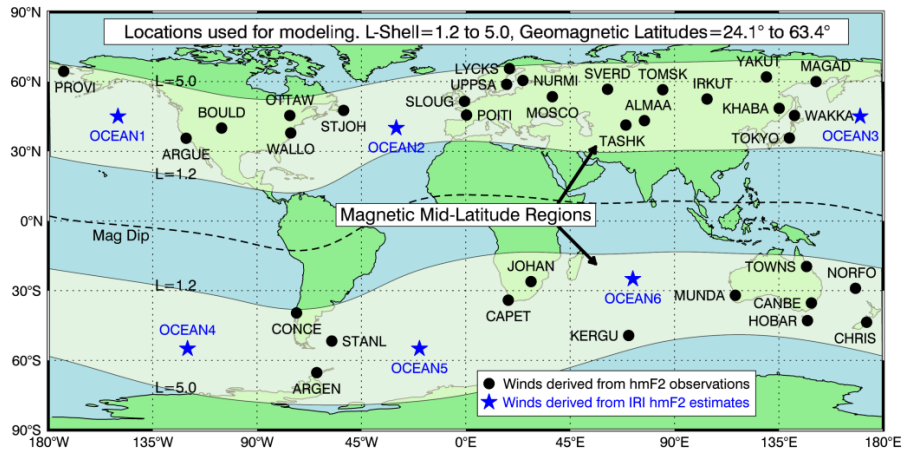


Figure 6.5. Map of the 40 ionosondes sites used to develop the new wind model. Ground-based sites are indicated with black circles. Ocean-based sites that derived winds from used IRI hmF2 are indicated with blue stars. The magnetic mid-latitude regions are indicated by the light-yellow strip in each hemisphere.

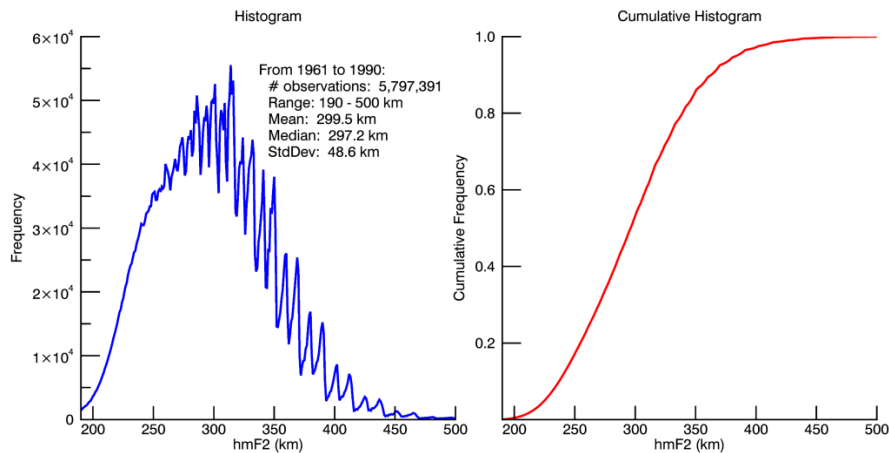


Figure 6.6. Distribution of the h_mF_2 observations from the ground-based sites in Table 6.1. The observations span the full years from 1961 to 1990. IRI h_mF_2 values from the six ocean locations were not included.

The FLIP model is written in Fortran and has several configuration files and dozens of configuration variables. Scripts were developed using the Interactive Data Language (IDL) that configured and executed the FLIP model to generate the equivalent winds at each site for one full year at a time. The scripts created a directory for each model run, copied all the required data and configuration files into each run directory, modified the FLIP configuration files for each run, executed each run, monitored the individual processes as they ran, reviewed the output files to make sure each job completed properly, and documented the overall progress of the meridional winds database. In all, a total of 2,686 year-long FLIP runs were executed for the database.

Even though the focus of the new empirical model is on the magnetic mid-latitude regions, many NGDC sites in the low- and high-latitudes were also processed to generate equivalent winds. This was done in part for posterity and because, once the automated data-processing scripts were in place, very little extra work was required. Some of the equatorial and polar winds may be investigated later for continuity over those regions and for comparisons with observations. The model runs were completed during off-hours after the meridional winds database had been developed.

The FLIP model was run on an Intel Core i7-3770K Ivy Bridge 3.5 GHz Quad-Core 77 Watt CPU with 32 GB (4 x 8 GB) Kingston DDR3 1600 RAM. The Core i7 CPU is hyperthreaded so it has four physical cores and eight logical cores. Running multiple FLIP jobs simultaneously often demanded 100% of the computer's resources for weeks at a time. Each year-long FLIP run took around 8 wall-clock hours to complete.

Generating the entire mid-latitude meridional wind database took 2,686 jobs x 8 wall-clock hours per run, or 21,488 wall-clock hours, or 2.45 wall-clock years. There were also unexpected events along the way (system crashes, etc.) that slowed things down. In all, it took more than 2.5 years to generate the entire wind database for empirical modeling.

6.3 Empirical Model Validation

The new empirical wind model has been given the name MENTAT, an acronym which stands for Magnetic mEridional NeuTrAl Thermospheric wind model. A comparison of raw modeled winds from FLIP, the new MENTAT empirically modeled winds, and HWM14 winds is shown in Figure 6.7. Four locations were selected that are located far from each other and in both hemispheres: (a) Boulder, (b) Magadan, (c) Canberra and (d) Johannesburg. The behavior of $h_m F_2$ and magnetic meridional neutral winds is shown for the same four consecutive days (March 1-4, 1990) at each location. In each upper plot, hourly $h_m F_2$ observations are represented by the green squares and the FLIP model $h_m F_2$ fit to the observations is shown as the thin black line. In each lower plot, the raw FLIP derived equivalent winds are shown as the thin black line, the MENTAT empirical model winds are shown as the thick blue line, and HWM14 empirical model winds are shown using the stippled red line. The FLIP model accurately reproduces the hourly $h_m F_2$ observations.

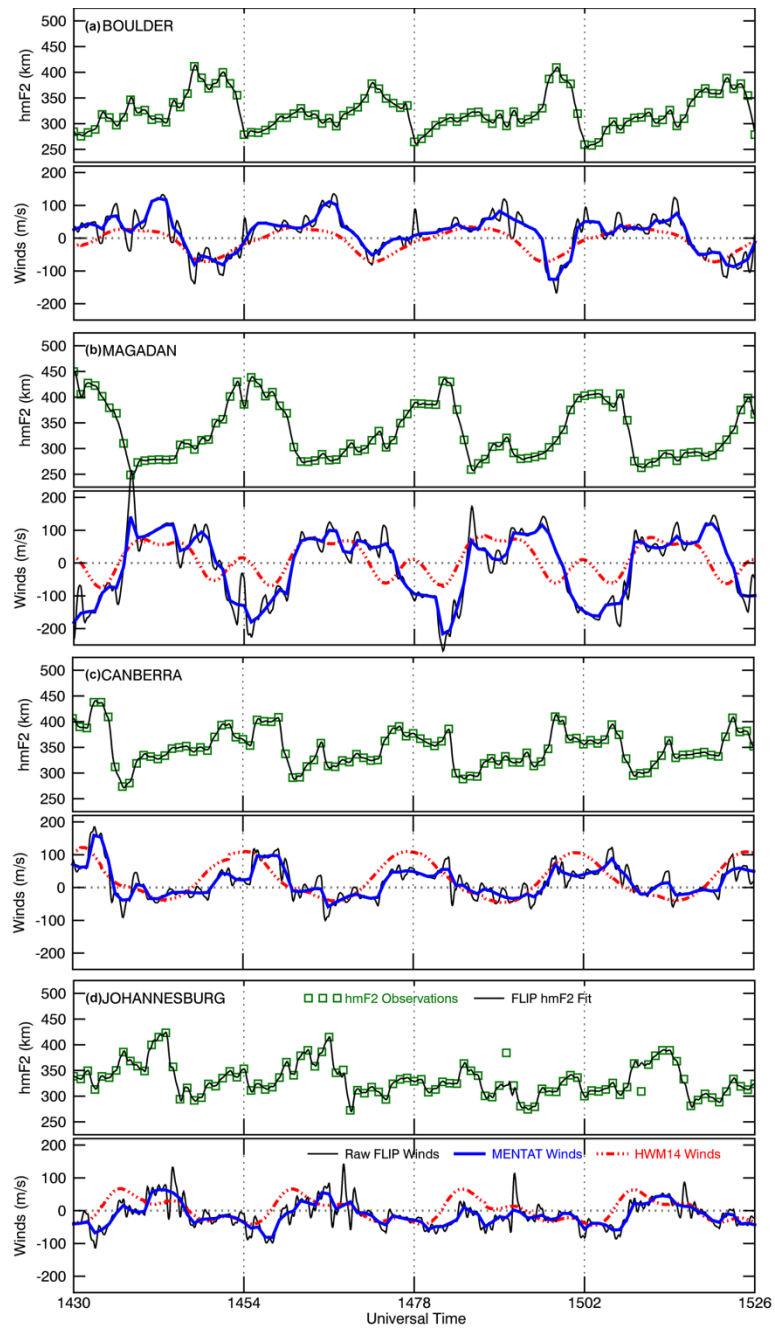


Figure 6.7. $h_m F_2$ and meridional neutral winds at four locations during March 1-4, 1990. Upper plots: ionosonde $h_m F_2$ observations (green squares) and FLIP model fit to them (black line). Lower plots: FLIP derived equivalent winds (solid black line), MENTAT modeled winds (thick blue line), and HWM14 modeled winds (stippled red line).

In each wind plot, the FLIP winds and MENTAT winds include the surges and abatements that are required to reproduce both the diurnal behavior of $h_m F_2$ and the hourly variability. The HWM14 winds do not exhibit the short-term variability to reproduce the hourly $h_m F_2$ observations. The HWM14 empirical winds exhibit the expected diurnal behavior at Boulder and Magadan and Canberra, but they appear to be a few hours out of phase at Johannesburg. At Johannesburg, the $h_m F_2$ data achieve a maximum about halfway between the vertical lines on the first, third and fourth days. The HWM14 winds on those days, however, achieve their maximum northward speed a few hours earlier on each day. If these HWM14 winds were being used to drive an ionospheric model at this location on these dates, the model would generate an incorrect specification of the ionosphere. The Johannesburg data exhibit the sunrise wind surge mentioned earlier, which is appropriately ignored by MENTAT.

MENTAT modeled winds are compared to with FPI wind observations and HWM14 winds in Figure 6.8. The MENTAT winds do not reproduce the FPI data quite as well as the equivalent winds that ingested IRI $h_m F_2$ (dashed black lines) in Figure 4.2(a), but they generally match the data better than the HWM14 winds (dotted red lines). The MENTAT winds reproduce the daily trend of the FPI data quite well at VTI and PAR locations. The MENTAT winds transition from northward to southward between 6:00 PM and 8:00 PM at each site, which is similar to the behavior of the FPI winds. The HWM14 wind speeds, on the other hand, do not change direction during that time period at any of the three locations.

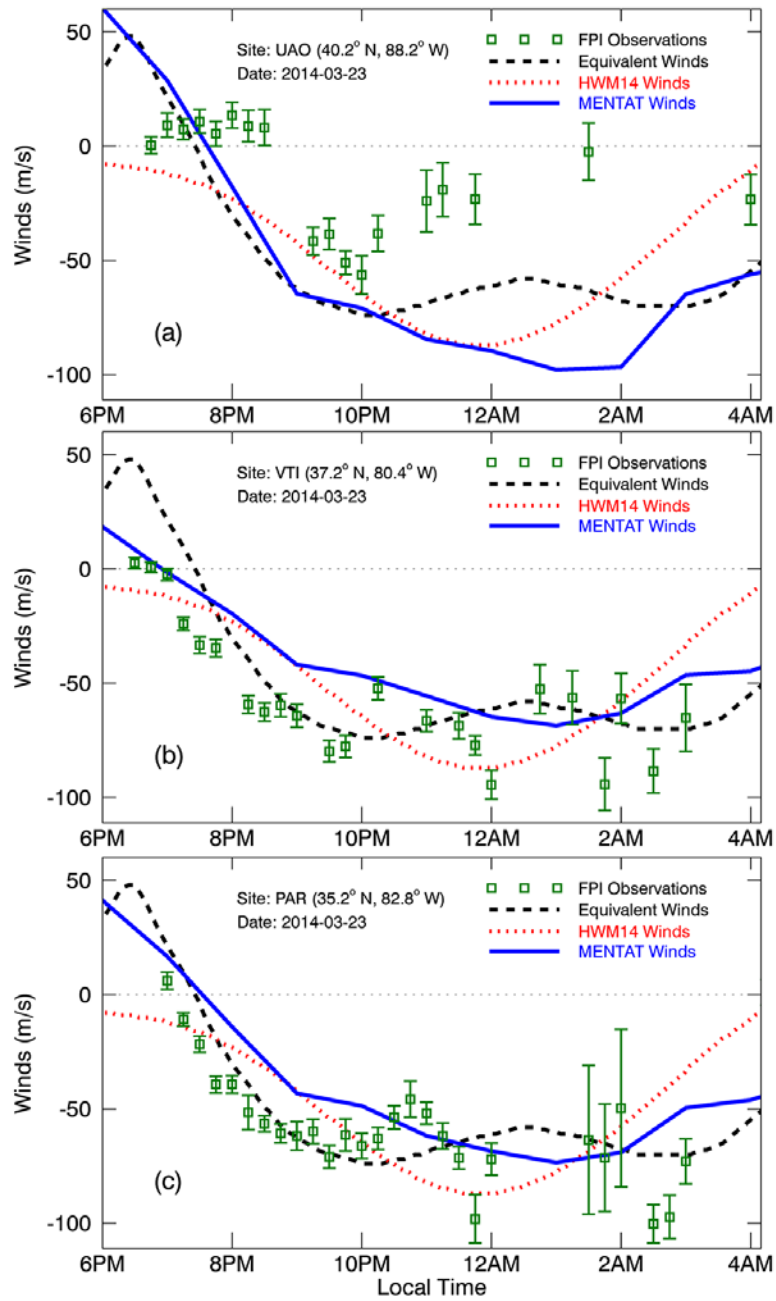


Figure 6.8. MENTAT modeled winds, HWM14 winds, and FPI observed winds at the three sites used in Chapter 4.

To evaluate long-term behavior of the MENTAT winds, the seasonal median comparisons with observed FPI winds shown in Figure 4.4 are repeated in Figure 6.9, but the MENTAT winds have replaced the raw modeled equivalent winds. Note that the MENTAT winds will be most influenced by the historical measurements from nearest ionosondes located at Wallops Island and Boulder. The median MENTAT winds (dashed black line) reproduce the median FPI winds (solid black line) better than the median HWM14 winds (blue lines) in the summer, fall and winter seasonal periods, apart from a few hours. However, the departure of the median equivalent wind from the median FPI wind that began around 1:00 AM in spring period in Figure 4.4(a) occurs once again with the MENTAT winds, as seen in Figure 6.9(a). In fact, the deviation of the MENTAT median wind from the FPI median wind begins much earlier, around 9:30 PM instead of 1:00 AM, and the difference between the two winds reaches nearly 100 m/s over the course of the night. The underlying statistics of the observed and modeled winds may explain why the MENTAT winds perform worse than HWM14 during a handful of hours in the summer, fall and winter periods, but the increasing difference in the spring period indicates a systematic error or bias and requires an in-depth investigation.

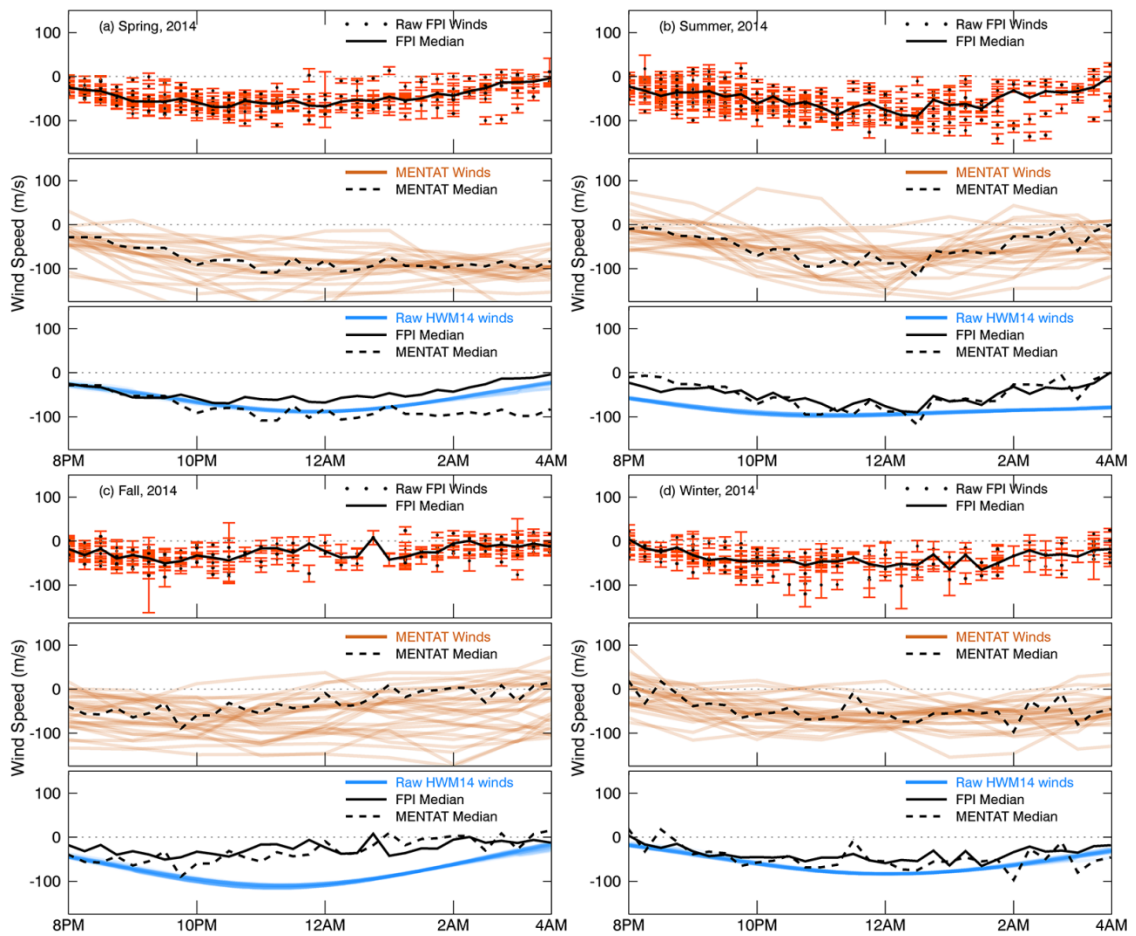


Figure 6.9. Observed and modeled seasonal (a, b, c, d) magnetic meridional neutral winds at PAR in 2014. Raw FPI wind observations with red error bars are shown in the top panes. MENTAT empirical winds are shown in brown in the center panes. Modeled HWM14 winds are shown in blue in the lower panes. Seasonal medians are shown as solid (FPI) and dashed (MENTAT) black lines. The FPI and MENTAT medians are repeated in the lower panes for comparison with HWM14 winds.

MENTAT modeled winds at Townsville (solid black line) and Arecibo (dashed red line) and HWM14 winds (stippled green line) at Townsville for eight days in February 1970 are shown in the top of Figure 6.10. The lower plot shows the resulting modeled $h_m F_2$ when each set of winds was input to the FLIP model as the data constraint. The

vertical blue lines show where the MENTAT winds are suddenly strongly downward and drive down the F2 layer at midnight local time, thus generating the midnight collapse. To make the plots easier to read, the Arecibo data set was shifted in time to line up local midnight with Townsville, and the Arecibo winds were negated so that the winds at both sites are in-phase. As shown on the map in Figure 6.5, there was relatively little ionosonde data in the Arecibo region, yet MENTAT was able to model a large midnight collapse of h_mF_2 . The HWM14 winds exhibit a long, slow abatement in the southward wind from sunset until around just before noon the next day, but they never become sufficient to sharply drive down the F2 layer at midnight and generate a midnight collapse. The HWM14 winds also never travelled southward over the eight-day period.

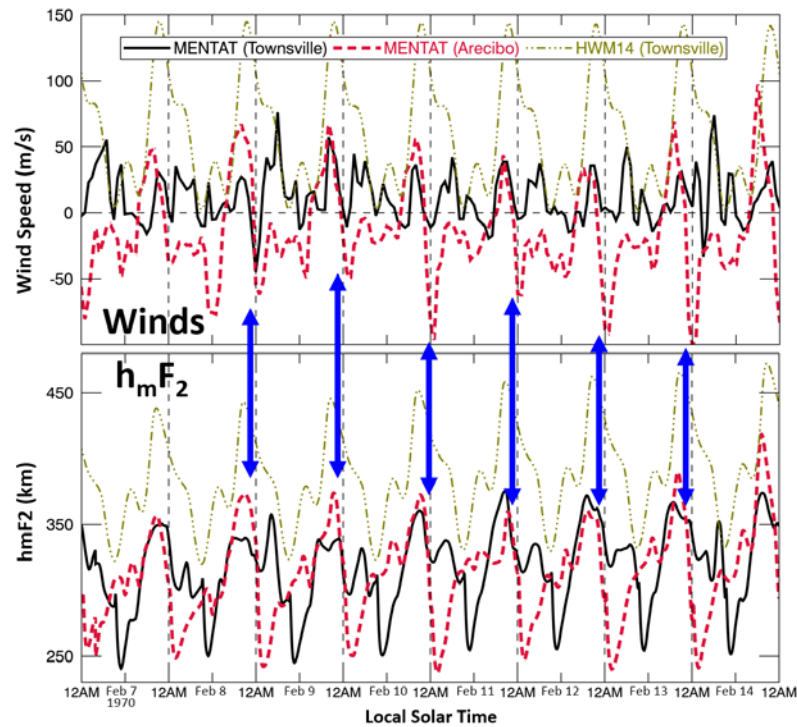


Figure 6.10. Top: MENTAT modeled winds at Townsville (solid black line) and Arecibo (dashed red line) and HWM14 winds (stippled green line) at Townsville. Bottom: Modeled $h_m F_2$ when using the winds from the top plot as the input to the FLIP model. The vertical blue lines show where the MENTAT winds are suddenly and strongly downward and driving down the F2 layer, thus creating the midnight collapse.

6.4 Empirical Model User Interface

This version of the MENTAT empirical model has been designed to generate global winds for any date and time after December 31, 1960. The comparison of modeled MENTAT winds with observed FPI winds in Figure 6.8 demonstrates how well MENTAT performs during one night in the year 2014 at three separate locations. Figure 6.9 demonstrates its capability during four seasonal periods at one location during the year 2014. When a User requests winds for a date beyond the maximum NGDC data

range (beyond 1990), the year (YY) and day of year (DDD) in each of the three decades of NGDC data (the 1960s, 1970s, and 1980s) are searched for an F10.7 value that most closely matches the User's F10.7 value. MENTAT determines the User's F10.7 value using a lookup table that is included as part of the MENTAT software package. The three F10.7 values from the three decades are compared to the User's F10.7 value and the value closest to the User's value defines the starting year for the modeled winds. For example, if a User requests a wind speed at 1300 UT on day of year 125 in the year 2017, the F10.7 value for that day will be retrieved from the lookup table. Let's say that the F10.7 value on day of year 125 in the year 2017 is 200 SFU. MENTAT will then look up the historical F10.7 values for day of year 125 in the three years 1967 (F10.7=90), 1977 (F10.7=135) and 1987 (F10.7=225). Of those three historical F10.7 values, the one that is closest to 200 SFU will define the starting year in the historical database to generate winds. In this example, the year 1977 would be selected since it has the closest F10.7 value (135) to the User's value (125). MENTAT would then generate winds for the User by using the globally interpolated winds from the year 1977 and day of year 125.

The day of year is used as the primary search key rather than F10.7 to make sure that recurring seasonal factors such as the local solar zenith angle, tidal effects, and the EUV-driven wind circulation patterns are accounted for in the modeled winds. Solar and geomagnetic activity dependencies are not explicitly included in this version of the model, but they may be included future versions. Solar activity has a relatively insignificant effect on thermospheric wind speeds during the day, but can be significant

at night. Geomagnetic activity can have a very strong impact on the thermospheric neutral winds, but the magnitude and timing of the impact at any specific location is a very complicated subject and beyond the scope of this research effort.

When a user requests a wind value from the MENTAT model, only temporal interpolation is required. Spatial interpolation (kriging) was done previously during the generation of the global winds database, to an output grid resolution of 5° latitude and 5° longitude. The 5° x 5° geographic grid resolution is dense enough to accommodate the full range of declination variability of meridional winds in the mid-latitudes. Each year of wind data is saved in a binary file that consists of 8760 hours of winds at 2,664 locations (a 5° x 5° global grid consists of 37 latitudes x 72 longitudes = 2,664 intersections.)

The MENTAT model interface was designed to mimic the HWM models. The input parameters are the same: GLAT and GLON for geographic location, YYDDD for the year and day of year, and UTSEC for the UT second within the day of year. As in the HWM model, the UTSEC values input to the model define the fractional times for wind interpolation. The MENTAT wind database has a one hour time resolution, but the model will interpolate winds to any fractional universal times. Figure 6.11 shows four days of MENTAT winds at 15-minute time resolution. The FLIP model winds are shown by the solid black line, the HWM14 wind is shown using the dashed red line, and the blue circles represent the MENTAT model winds with a 15-minute resolution. The high-resolution MENTAT winds behave as expected over the full period.

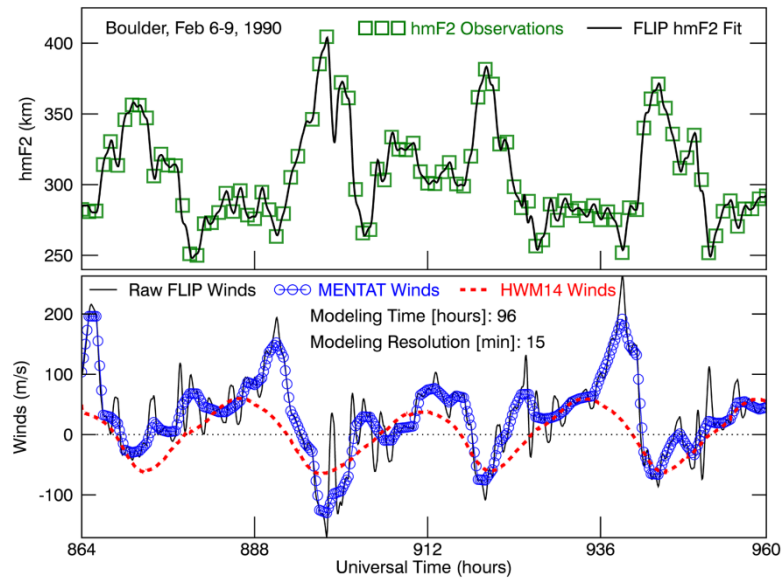


Figure 6.11. Four days of modeled MENTAT winds using a 15-minute time resolution. Raw FLIP winds are shown using the thin black line. HWM14 winds use the dashed red line. The MENTAT winds are shown using the blue circles.

However, the MENTAT model is designed differently from the HWM models in one significant way. The HWM model uses scalar values for its input parameters and output value. It needs to be called N times to get N wind values, which can be tedious and inefficient. Instead, MENTAT uses arrays for its input parameters and output values. The input data for MENTAT should be set up as string arrays to allow for leading zeroes in the date fields (e.g., YYDDD = "05003" for year 2005 and day of year 3.) Using this approach, when equivalent winds are needed for multiple locations and/or times, MENTAT only needs to be called once with all the date and time parameters in the input arrays. The MENTAT model output will be a numeric array of the same length containing the wind speed for each input location & time. This approach creates a simpler interface

and, since fewer individual model calls are required, it is a much more efficient design. If a wind is required at only a single location/date/time, then each input array should contain just one data element. This approach will also make it easier to drive the model from data in a simple ASCII file.

CHAPTER 7: CONCLUSION

The research in this dissertation will contribute to the ionospheric physics and space weather communities in significant ways. Accurate quantitative modeling of F region densities is not possible without an accurate specification of magnetic meridional neutral winds in the thermosphere. A solid understanding of the coupling between the neutral winds of the thermosphere and the ionosphere is critical to understanding ionospheric dynamics.

The work in this dissertation describes the construction of and validation of an equivalent neutral winds derived from observed variations of $h_m F_2$. Examples in Chapter 4 demonstrated that the equivalent winds do very well when compared to Fabry-Perot interferometer (FPI) optical observations and that they generally perform better than empirical HWM14 winds. The equivalent winds matched the individual FPI observations at three different locations very well in terms of direction and magnitude and they were a better match to the data than HWM14 winds.

Chapter 4 also demonstrated that median equivalent winds are much closer to median FPI observations than median HWM14 winds over month-long seasonal periods. The meridional winds performed better in each 8 PM to 4 AM period except for the hours from 2 AM to 4 AM in the spring, fall and winter. However, since the IRI $h_m F_2$ was

used to drive the FLIP model in these cases, these deviations in the equivalent winds may be due to systematically high values of IRI h_mF_2 in those early morning hours. These comparisons also demonstrated that there is very little day-to-day variability in the HWM empirical winds. The daily spread in the modeled equivalent winds is much more like the daily spread in the observed FPI winds.

Chapter 5 showed an example of the equivalent winds used for a recent scientific paper. The midnight collapse of the ionosphere was identified as a regular phenomenon at Townsville, which is geographically and geomagnetically similar to Arecibo, where the collapse occurs regularly. By comparing equivalent winds at magnetically conjugate stations, it was shown that electric fields do not play a significant role in the collapse. The midnight collapse occurred on 89% of the observed nights at Townsville, which is very close to the documented 85% rate at Arecibo. Using hourly h_mF_2 observations, continuous equivalent winds were generated from 1970 to 1980 for the March and September equinox periods and a spectral analysis was done. The power spectral densities of the 24-, 12-, 8-, and 6-hour tidal components in both seasons showed a strong anti-correlation with solar flux, and the relative strengths of each tide was generally the same in each season. To isolate the tidal components that are responsible for the midnight collapse, the equivalent winds were combined sequentially, and then ingested by FLIP to determine how the tidal components affect h_mF_2 around midnight. The results showed that the interaction of the first three tidal components are

the primary drivers for the midnight collapse and that the contribution of the terdiurnal wind component is minor.

Chapter 6 described how an equivalent winds database was built from 30 years of winds at 40 locations in the magnetic mid-latitudes in order to develop a new empirical model; the Magnetic meridional Neutral Thermospheric (MENTAT) wind model. MENTAT winds were shown to include the surges and abatements required to reproduce the diurnal and hourly variability behavior of $h_m F_2$. The individual FPI comparisons from Chapter 4 were repeated and the MENTAT winds were shown to be closer to the FPI winds than HWM14 winds. The seasonal median comparisons with FPI winds from Chapter 4 were also repeated using the MENTAT winds. Apart from a handful of hours, the median FPI winds performed better than the median HWM14 winds in the summer, fall and winter periods, and for roughly half of the spring period.

The MENTAT software architecture was designed with users of the HWM model in mind. Its user interface is similar to the user interface of the HWM models so that the models may be easily interchanged. MENTAT will generate winds for any date and time after December 31, 1960, at any geographic latitude and longitude. The model was designed for speed and it should be straightforward to port to other programming languages.

The findings of this research will improve our fundamental understanding of thermospheric winds and, in turn, our understanding of ionospheric electron density variability. Empirical models have proven to be extremely important to progress in

space science, and the MENTAT model should prove be a very useful tool for ionospheric researchers. This research will improve progress in understanding the fundamental physical processes of the space environment from the sun to Earth, and from the sun to other magnetized planets. It should also improve progress in understanding how human society, technological systems, and the habitability of planets are affected by solar variability interacting with planetary magnetic fields and atmospheres.

CHAPTER 8: FUTURE WORK

The development of the MENTAT wind model creates many opportunities for future research. Potential research papers include investigating the seasonal and solar cycle variations of the meridional neutral winds, comparing MENTAT winds with HWM14 winds in various scenarios, and investigating the effects of geomagnetic activity on MENTAT winds compared to HWM14 (DWM) winds. A scientific campaign where one or more FPIs are co-located with one or more ionosphere sounders or incoherent scatter radars at mid-latitudes would be productive.

It would be informative to develop a new version of the model using the Bilitza method for modeling $h_m F_2$ (rather than the Dudeney method for $h_m F_2$) and compare the wind differences. A climatological or 'quiet time' version of the MENTAT model built using $h_m F_2$ from IRI could prove useful. Comparing quiet time meridional winds with storm-time meridional winds may prove useful for investigating the effects of geomagnetic storms (strong Kp) on winds. The MENTAT model winds may be integrated into an updated HWM model once the equivalent winds are proven to be compatible with, and complementary to, the HWM winds. We could also examine systematic differences between the two models, which may indicate the importance of electric fields. It's possible that accurate, near-real-time $h_m F_2$ data may be used as the input to a

version of MENTAT to estimate local thermospheric wind speeds in near-real-time. Co-located ionosondes and FPI instruments would be required for development and testing, but only ionosondes may be required for operational use.

It may be possible to break the magnetic meridional winds into geographic zonal and meridional winds by using the fact that the equivalent winds are purely meridional when the declination is small. We would estimate the total zonal winds at other longitudes from the formula $W_{eq} = W_{zon} \times \sin D + W_{mer} \times \cos D$, where W_{eq} is the FLIP (or MENTAT) model equivalent wind, W_{zon} is the zonal component to be estimated, W_{mer} is the FLIP model meridional component, and D is the local magnetic declination.

A seasonal conjugate wind study may help quantify seasonal mean flow rates from the summer hemisphere to the winter hemisphere. Investigating the equivalent winds for cross-region continuity in the high-latitude and equatorial regions would be interesting. The Kriging approach used for global interpolation of the MENTAT winds provides wind continuity over these regions, but winds there are uncertain and need to be compared to observed FPI winds for validation.

REFERENCES

- Akmaev, R. A., F. Wu, T. J. Fuller-Rowell, and H. Wang (2009), Midnight temperature maximum (MTM) in Whole Atmosphere Model (WAM) simulations, *Geophys. Res. Lett.*, 36, L07108, doi:10.1029/2009GL037759.
- Akmaev, R. A., F. Wu, T. J. Fuller-Rowell, H. Wang, and M. D. Iredell (2010), Midnight density and temperature maxima, and thermospheric dynamics in Whole Atmosphere Model simulations, *J. Geophys. Res.*, 115, A08326, doi:10.1029/2010JA015651.
- Behnke, R. A., and R. M. Harper (1973), Vector measurements of F region ion transport at Arecibo, *J. Geophys. Res.*, 78, 8222–8234, doi:10.1029/JA078i034p08222.
- Bilitza, D., N. M. Sheikh, and R. Eyrig (1979), A global model for the height of the F2-peak using M3000 values from the CCIR numerical map, *Telecom J.*, 46, 549–553.
- Bilitza, D., Comparison of measured and predicted F2 peak altitudes, *Adv. Space Res.* 5, #10, 29 - 32, 1985.
- Bilitza, D., D. Altadill, V. Truhlik, V. Shubin, I. Galkin, B. Reinisch, and X. Huang (2017), International Reference Ionosphere 2016: From ionospheric climate to real-time weather predictions, *Space Weather*, 15, 418–429, doi:10.1002/2016SW001593.
- Bilitza D., D. Altadill, Y. Zhang, C. Mertens, V. Truhlik, P. Richards, L.-A. McKinnell, and B. Reinisch: The International Reference Ionosphere 2012 – a model of international collaboration. *J. Space Weather Space Climate*, 4, A07, 1-12, doi:10.1051/swsc/2014004, 2014.
- Bremer, J. (1992), Ionospheric trends in midlatitudes as a possible indicator of the atmospheric greenhouse effect, *J. Atmos. Terr. Phys.*, 54, 1505–1511.
- Bremer J., Alfonsi L., Bencze, P., *Laštovička*, J., Mikhailov A.V., Rogers, N., Long-term trends in the ionosphere and upper atmosphere parameters, *Annals of Geophysics*, Supplement To Vol. 47, N. 2/3, 2004.

- Burnside, R. G., C. A. Tepley, and V.B. Wickwar, The O⁺-O collision cross-section: Can it be inferred from aeronomical measurements?, *Ann. Geophys., Ser. A*, 5 (6), 343, 1987.
- Buonsanto, M. J., J. E. Salah, K. L. Miller, W.L. Oliver, R. G. Burnside, and P. G. Richards, Observations of Neutral Circulation at Mid-Latitudes during the Equinox Transition Study, *J. Geophys. Res.*, 94, 12, 16,987-16,997, 1989.
- Buonsanto, M. J., M. J. Starks, J. E. Titheridge, P. G. Richards, and K. L. Miller, Comparison of techniques for derivation of neutral meridional winds from ionospheric data, *J. Geophys. Res.*, 102, 14,477, 1997a.
- Buonsanto, M. J., D. P. Sipler, G. B. Davenport, and J. M. Holt, Estimation of the O⁺, O collision frequency from coincident radar and Fabry-Perot observations at Millstone Hill, *J. Geophys. Res.*, 102, 17, 267, 1997b.
- Burnside, R. G., J. W. Meriwether, and M. R. Torr (1977), Contamination of ground-based measurements of OI (6300Å) and NI (5200Å) airglow by OH emissions, *Planet. Space Sci.*, 25, 985– 988, doi:10.1016/0032-0633(77)90012-5.
- Burnside, R. G., and C. A. Tepley (1990), Airglow intensities observed in the southern and northern hemispheres, *Planet. Space Sci.*, 38, 1161–1177, doi:10.1016/0032-0633(90)90024.
- Crary, D. J., and J. M. Forbes (1986), The dynamic ionosphere over Arecibo: A theoretical investigation, *J. Geophys. Res.*, 91, 249–258, doi:10.1029/JA091iA01p00249.
- Dandenault, P. B., and P. G. Richards (2015), The collapse of the midnight ionosphere and behavior of meridional neutral winds at Townsville over a full solar cycle, *J. Geophys. Res. Space Physics*, 120, doi:10.1002/2015JA021842.
- Drob, D. P., J. T. Emmert, G. Crowley, J. M. Picone, G. G. Shepherd, W. Skinner, P. Hays, R. J. Niciejewski, M. Larsen, C. Y. She, J. W. Meriwether, G. Hernandez, M. J. Jarvis, D. P. Sipler, C. A. Tepley, M. S. O'Brien, J. R. Bowman, Q. Wu, Y. Murayama, S. Kawamura, I. M. Reid, and R. A. Vincent, An empirical model of the Earth's horizontal wind fields: HWM07, *J. Geophys. Res.*, 113, 2008.
- Drob, D. P. et al. (2015), An Update to the Horizontal Wind Model (HWM): The Quiet Time Thermosphere, *Earth and Space Science*, 2, doi:10.1002/2014EA000089.

- Dudenev, J. R. (1974), A simple empirical method for estimating the height and semithickness of the F2-layer at the Argentine Islands, *Sci. Rep.* 88, British Antarct. Surv., Cambridge, U.K.
- Dudenev, J.R., The accuracy of simple methods for determining the height of the maximum electron concentration of the F2-layer from scaled ionospheric characteristics, *J. Atmos. Terr. Phys.*, 45, 629, 1983.
- Dyson, P. L., T. P. Davies, M. L. Parkinson, A. J. Reeves, P. G. Richards, and C. E. Fairchild, Thermospheric neutral winds at southern mid-latitudes: A comparison of optical and ionosonde hmF2 methods, *J. Geophys. Res.*, 102, 27189, 1997.
- ESRI 1999, ArcGIS Software Interpolation toolset concepts, accessed 1 May 2017, 'How Kriging works', <<http://desktop.arcgis.com/en/arcmap/latest/tools/3d-analyst-toolbox/how-kriging-works.htm>>
- Evans, J. V., A study of F2 region daytime vertical ionization fluxes at Millstone Hill during 1969, *Planet. Space Sci.*, 23, 1461, 1975.
- Hanson, W. B., and T. N. Patterson, The maintenance of the night-time F-layer, *Planet Space Sci.*, 12, 979-997, 1964.
- Harper, R. M. (1979), A semidiurnal tide in the meridional wind at F region heights at low latitudes, *J. Geophys. Res.*, 84, 411–415, doi:10.1029/JA084iA02p00411.
- Hedin, A. E., A revised thermospheric model based on mass spectrometer and incoherent scatter data: MSIS-83, *J. Geophys. Res.*, 88, 10170, 1983.
- Hedin, A. E., MSIS-86 thermosphere model, *J. Geophys. Res.*, 92, 4649, 1987.
- Hedin, A. E., N. W. Spencer, and T. L. Killeen, Empirical global model of upper thermosphere winds based on Atmosphere and Dynamics Explorer satellite data, *J. Geophys. Res.*, 93, 9959, 1988.
- Hedin, A. E., M. A. Biondi, R. G. Burnside, G. Hernandez, R. M. Johnson, T. L. Killeen, C. Mazaudier, J. W. Meriwether, J. E. Salah, R. J. Sica, R. W. Smith, N. W. Spencer, V. B. Wickwar, and T. S. Virdi, Revised global model of thermospheric winds using satellite and ground-based observations, *J. Geophys. Res.*, 96, 7657, 1991.

- Hedin, A. E., E. L. Fleming, A. H. Manson, F. J. Schmidlin, S. K. Avery, R. R. Clark, S. J. Franke, G. J. Fraser, T. Tsuda, F. Vial, and R. A. Vincent, Empirical wind model for the upper, middle and lower atmosphere, *J. Atmos. Terr. Phys.*, 58, 1421, 1996.
- Immel, T. J., E. Sagawa, S. L. England, S. B. Henderson, M. E. Hagan, S. B. Mende, H. U. Frey, C. M. Swenson, and L. J. Paxton, Control of equatorial ionospheric morphology by atmospheric tides, *Geophys. Res. Lett.*, 33, L15108, doi:10.1029/2006GL026161, 2006.
- Larsen, M. F., Winds and shears in the mesosphere and lower thermosphere: Results from four decades of chemical release wind measurements, *J. Geophys. Res.*, 107, A8, 1215, doi:10.1029/2001JA000218, 2002.
- Larsen, M. F., and J. W. Meriwether (2012), Vertical winds in the thermosphere, *J. Geophys. Res.*, 117, A09319, doi:10.1029/2012JA017843.
- Lee, J. S., J.P. Doering, T. A. Potemra, and L. H. Brace, Measurements of the ambient photoelectron spectrum from Atmosphere Explorer, I, AE-E measurements below 300 km during solar minimum conditions, *Planet. Space Sci.*, 88, 947, 1980.
- Macpherson, B., S. A. González, G. J. Bailey, R. J. Moffett, and M. P. Sulzer (1998), The effects of meridional neutral winds on the O⁺-H⁺ transition altitude over Arecibo, *J. Geophys. Res.*, 103, 29,183–29,198, doi:10.1029/98JA02660.
- Makela J. J., Meriwether J. W., Ridley A. J., Ciocca M., and Castellez, M.W., Large-Scale Measurements of Thermospheric Dynamics with a Multisite Fabry-Perot Interferometer Network: Overview of Plans and Results from Midlatitude Measurements, *International Journal of Geophysics*, Volume 2012, Article ID 872140, doi:10.1155/2012/872140
- Makela, J. J., et al. (2014), Storm time response of the midlatitude thermosphere: Observations from a network of Fabry-Perot interferometers, *J. Geophys. Res. Space Physics*, 119, 6758-6773, doi:10.1002/2014JA019832.
- McNamara, L. F. (2008), Accuracy of models of hmF2 used for long-term trend analyses, *Radio Sci.*, 43, RS2002, doi:10.1029/2007RS003740.
- Mende, S. B., G. R. Swenson, and S. P. Geller (1993), Limb view spectrum of the Earth's airglow, *J. Geophys. Res.*, 98(A11), 19,117 – 19,125, doi:10.1029/93JA02282.

- Miller, K. L., D. G. Torr, and P. G. Richards, Meridional winds in the thermosphere derived from measurement of F2 layer height, *J. Geophys. Res.*, 91, 4531, 1986.
- Miller, K. L., J. E. Salah, and D. G. Torr, The effect of electric fields on measurements of meridional neutral winds in the thermosphere, *Ann. Geophys.*, 5A, 337-342, 1987.
- Miller, K. L., R. L. Breninger, P. G. Richards, and D. G. Torr, The solar cycle variation of meridional neutral winds in the thermosphere, *EOS.*, 70, 1243, 1989.
- Miller, K. L., P. G. Richards, and H. Y. Wu, A global study of meridional winds and electron densities in the F-region during the SUNDIAL 1987 campaign, *Ann. Geophys.*, 11, 572, 1993.
- Nagy, A. F., and P.M. Banks, Photoelectron fluxes in the ionosphere, *J. Geophys. Res.*, 75, 6260, 1970.
- Nelson, G. J., and L. L. Cogger (1971), Dynamical behavior of the nighttime ionosphere at Arecibo, *J. Atmos. Sol. Terr. Phys.*, 33, 1711–1726, doi:10.1016/0021-9169(71)90219-4.
- Newberry, I. T., R. H. Comfort, and P. G. Richards, Thermal He⁺ in the plasmasphere: Comparison of observations with numerical calculations, *J. Geo Phys. Res.*, 94, 15, 265, 1989.
- Nicolls, M. J., N. Aponte, S. A. Gonzalez, M. P. Sulzer, and W. L. Oliver, Daytime F region ion energy balance at Arecibo for moderate to high solar flux conditions, *J. Geophys. Res.*, 111, A10307, doi:10.1029/2006JA011664, 2006.
- Picone, J. M., A. E. Hedin, D. P. Drob, and A. C. Aikin, NRLMSISE-00 empirical model of the atmosphere: Statistical comparisons and scientific issues, *J. Geophys. Res.*, 107(A12), 1468, doi:10.1029/2002JA009430, 2002.
- Richards, P. G., and D. G. Torr, An investigation of the consistency of the ionospheric measurements of the photoelectron flux and solar EUV flux, *Geophys. Res.*, 89, 5625, 1984.
- Richards, P. G., and D. G. Torr, A factor of 2 reduction in the theoretical F2 peak electron density due to enhanced vibrational excitation of N₂ in summer at solar maximum, *Y. Geophys. Res.*, 91, 11,331, 1986.

- Richards, P. G., and D. G. Torr, Ratios of photoelectron EUV ionization rates for aeronomic studies, *J. Geophys. Res.*, 93, 4060, 1988.
- Richards, P. G., D. G. Torr, M. J. Buonsanto and K. L. Miller, The behavior of the electron density and temperature at Millstone Hill during the Equinox Transition Study September 1984, *J. Geophys. Res.*, 94, 16, 969, 1989.
- Richards, P. G., An improved algorithm for determining neutral winds from the height of the F2 peak electron density, *J. Geophys. Res.*, 96, 17,839, 1991.
- Richards, P. G., D. G. Torr, B. W. Reinisch, R. R. Gamache, and P. J. Wilkinson, F2 peak electron density at Millstone Hill and Hobart: Comparison of theory and measurement at solar maximum, *J. Geophys. Res.*, 99, 15,005, 1994.
- Richards, P. G., D. G. Torr, M. J. Buonsanto, and D. W. Sipler, Ionospheric effects of the March 1990 magnetic storm: Comparison of theory and measurement, *J. Geophys. Res.*, 99, 23,359, 1994.
- Richards P. G., D. G. Torr, M. E. Hagan, and M. J. Buonsanto, A new algorithm for improved ionospheric electron density modeling, *Geophys. Res. Lett.*, 22, 1385, 1995.
- Richards, P. G., and P. J. Wilkinson, The ionosphere and thermosphere at southern mid-latitudes during the November 1993 ionospheric storm: A comparison of measurement and modeling, *J. Geophys. Res.*, 103, 9373, 1998a.
- P. G. Richards P. L. Dyson, T. P. Davies, M. L. Parkinson, A. J. Reeves, Behavior of the ionosphere and thermosphere at a southern midlatitude station during magnetic storms in early March 1995, *J. Geophys. Res.*, 102, 26241, 1998b.
- Richards, P. G., Seasonal and solar cycle variations of the ionospheric peak electron density: Comparison of measurement and models, *J. Geophys. Res.* 106, 12,803, 2001.
- Richards, P. G., M. J. Nicolls, C. J. Heinselman, J. J. Sojka, J. M. Holt, and R. R. Meier, Measured and Modeled Ionospheric densities, temperatures, and winds during the IPY, *J. Geophys. Res.*, 114, A12317, doi:10.1029/2009JA014625, 2009.
- Richards, P. G., R. R. Meier, and P. J. Wilkinson, On the consistency of satellite measurements of thermospheric composition and solar EUV irradiance with

- Australian ionosonde electron density data, *J. Geophys. Res.*, 115, A10309, doi:10.1029/2010JA015368, 2010.
- Rishbeth, H., and D. W. Barron, Equilibrium electron distributions in the ionospheric F2-layer, *J. Atmos. Terr. Phys.*, 18, 234-252, 1960.
- Rishbeth, H., F2-Layer rates at sunspot minimum, *J. Atmos. Terr. Phys.*, 28, 911-918, 1966.
- Rishbeth, H., The effects of winds on the ionospheric F2-peak, *J. Atmos. Terr. Phys.*, 29, 225-238, 1967.
- Rishbeth, H., S. Ganguly, and J. C. G. Walker, Field-aligned and field-perpendicular velocities in the ionospheric F2-layer, *J. Atmos. Terr. Phys.*, 40, 767-784, 1978.
- Rishbeth, H., Thermospheric winds and the F-region: A review, *J. Atmos. Terr. Phys.*, 34, 1, 1972.
- Ruan, H., J. Lei, X. Dou, W. Wan, and Y. C.-M. Liu (2014), Midnight density maximum in the thermosphere from the CHAMP observations, *J. Geophys. Res. Space Physics*, 119, doi:10.1002/2013JA019566.
- Salah, J. E., Interim standard for the ion-neutral atomic oxygen collision frequency, *Geophys. Res. Lett.*, 20, 1543, 1993.
- Schunk, R. W., and A. F. Nagy, Electron temperatures in the F region of the ionosphere: Theory and observations, *Geophys.*, 16,355, 1978.
- Schunk, R. W., and J. G. Walker, Theoretical ion densities in the lower ionosphere, *Planet. Space Sci.*, 21, 1875, 1973.
- Scorer, R. S. (1992), *Atmospheric data analysis*, Roger Daley, Cambridge Atmospheric and Space Science Series, Cambridge University Press, Cambridge, 1991. No. of pages: xiv + 457. ISBN 0521 382157. *Int. J. Climatol.*, 12: 763–764. doi:10.1002/joc.3370120708
- Seker, I., D. J. Livneh, and J. D. Mathews (2009), A 3-D empirical model of F region medium scale travelling ionospheric disturbance bands using incoherent scatter radar and all-sky imaging at Arecibo, *J. Geophys. Res.*, 114, A06302, doi:10.1029/2008JA014019.

- Shimazaki, T. "World wide daily variations in the height of the maximum electron density in the ionospheric F2 layer." *J. Radio Res. Labs., Japan* 2.7 (1955): 86-97.
- St. Maurice, J.-P., and R. W. Schunk, Diffusion and heat flow equations for the mid-latitude topside ionosphere, *Planet. Space Sci.*, 85 ,907, 1976.
- Torr, M. R., D. G. Torr, P. G. Richards, and S. P. Yung, Mid- and low-latitude model of thermospheric emissions, 1, O⁺(2P) 7320 Å and N₂ (2P) 3371 Å, *J. Geophys. Res.*, 95, 21,147, 1990.
- Vasseur, G. (1969), Dynamics of the F region observed with Thomson scatter— I. Atmospheric circulation and neutral winds, *J. Atmos. Terr. Phys.*, 31, 397–420.
- Vlasov, M. N., M. J. Nicolls, M. C. Kelley, S. M. Smith, N. Aponte, and S. A. González (2005), Modeling of airglow and ionospheric parameters at Arecibo during quiet and disturbed periods in October 2002, *J. Geophys. Res.*, 110, A07303, doi:10.1029/2005JA011074.

BIOGRAPHY

Patrick Bryan Dandenault is done with college. Finally.